Clumped isotope (Δ_{47}) record of ODP Site 1263, Walvis Ridge: deep-sea temperatures during the Eocene-Oligocene Transition

GEO4-1520 MSc Thesis

M.T. (Maarten) Bosman
8470367
Utrecht University
Department of Earth Sciences

Final version: 26-08-2023

Supervisors
Prof. Dr. Lucas J. Lourens
Dr. Martin Ziegler
Tobias Agterhuis, MSc

Abstract

This study aims to reconstruct deep-sea temperatures at site 1263 on the Walvis Ridge in the South Atlantic Ocean during the Eocene-Oligocene Transition (EOT). The clumped isotope Δ_{47} thermometer is used on the benthic foraminifera species *Oridorsalis umbonatus*, *Cibicidoides havanensis* and *Cibicidoides spp*. The derived Δ_{47} temperatures are compared to the traditional proxies used for temperature reconstructions, i.e. with temperatures derived by stable $\delta^{18}O$ isotopes, Mg/Ca and TEX_{86} data. This study finds significant differences between temperature reconstructions based on different proxies and show the uncertainties and complications for each method. A temperature increase of ±3.9 °C (Meinicke calibration) and ±4.1 °C (Peral calibration) during the EOT using the clumped isotope thermometer has been found, unlike the traditional proxies that indicate a temperature decrease during the EOT. The clumped isotope (Δ_{47}) thermometer is independent on seawater chemistry and foraminifera physiology, unlike oxygen isotopes and Mg/Ca ratio proxies, making it an interesting proxy for a revision of the traditional assumptions. These findings challenge previous theories about the presence of ice sheets and provides evidence for the presence and extension of ice sheets during the EOT. Other factors that may contribute to fluctuations in oxygen isotope compositions of seawater ($\delta^{18}O_{sw}$), like salinity variations, aquifer-eustasy and seafloor spreading rates are also discussed. This research highlights importance of using multiple proxies and considering various factors when reconstructing temperatures.

Table of contents

Introduction

1.1 Climate during the Eocene – Oligocene transition

The global climate is rapidly changing due to anthropogenic influences. Increased carbon emissions of humans since the pre-industrial has resulted in changes in the atmosphere, ocean, cryosphere and biosphere (Change, 1990). It is expected that atmospheric carbon reaches levels close to the Paleocene-Eocene Thermal Maximum (PETM) in the future, resulting in increased uptake of CO_2 by the oceans, therefore acidification of oceans and a major global mean temperature increase (Zachos et al., 2008). It is certain that humanity will have to face major challenges if the emission of greenhouse gases is not limited. However, the exact response of the climate system to this carbon emission increase is highly uncertain (Zachos et al., 2008).

In order to predict future climate scenarios as accurate as possible, a good understanding of the past is essential. Deep-sea temperatures are commonly used to derive the global climate during a certain period, since the deep ocean is spatially constant in temperature and considered a stable element in the climate system compared to sea surface water (Agterhuis et al., 2022). This study will focus on reconstructing the deep-sea temperatures at the Walvis Ridge site 1263 during the Eocene-Oligocene Transition (EOT; 33.9 Ma – 32.5 Ma).

The EOT is characterized by major shifts in geochemical and sedimentological proxies (Coxall & Pearson, 2007). During this interval, an abrupt transition from a greenhouse world to an icehouse world occurred, resulting in a sudden increase of $\delta^{18}O$ from 1.4‰ to 2.4‰ and an increase in $\delta^{13}C$ from 0.3‰ to 1.4 ‰ as seen in benthic foraminifera records (Figure 1; Lear et al., 2008). The EOT marks a critical transition in global climate since atmospheric CO_2 declined, the deep-sea cooled and Antarctic ice sheet formed because of isolation of Antarctica (Katz et al., 2008). This resulted in rapid biotic changes and even extinctions of marine organisms (Prothero, 1994).

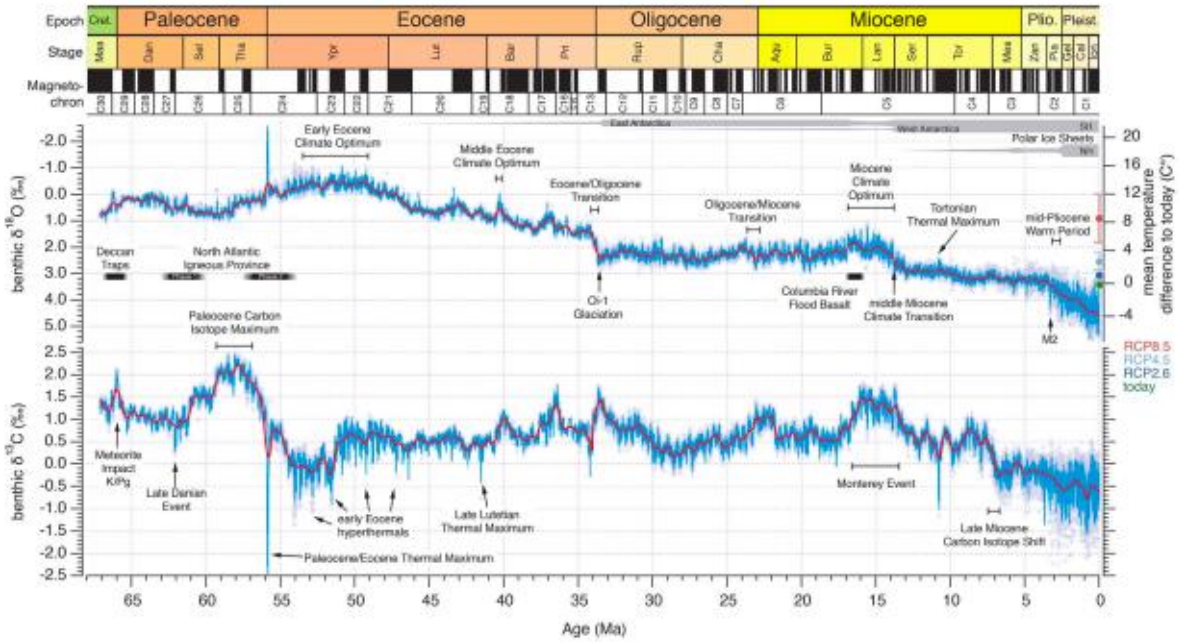

Figure 1.1: Cenozoic benthic foraminifer carbon and isotope dataset over past 66 million years (Westerhold et al., 2020)

1.2 Clumped isotope thermometry

Most climate reconstructions of the EOT are based on the stable oxygen and carbon isotopes of foraminifera, where high $\delta^{18}O$ values are indicative of lower temperatures (Katz et al., 2008). However, these oxygen isotope records represent a combined signal of deep-sea temperature and the isotope composition of the seawater, which latter mainly depends on the amount of ice volume (Ravelo & Hillaire-Marcel, 2007). Oxygen isotope records are commonly used in combination with Mg/Ca records as a paleotemperature proxy, but recent studies have revealed several complications regarding this proxy. At cold bottom water temperatures (i.e. below 5°C) salinity seems to be in control of the Mg/Ca ratio preserved in benthic foraminiferal tests, making it an unreliable proxy during cold periods (Evans & Müller, 2012). TEX_{86} is also used as a proxy to reconstruct temperatures, although this proxy is commonly used to reconstruct sea surface temperatures instead of deep-sea temperatures. TEX_{86} can be affected by genetic differences of the organisms that produce the lipid biomarkers and therefore is not reliable either (Conte et al., 1995). However, comparing sea surface temperatures with deep-sea temperatures can give an interesting insight in the global trend. Instead of using these proxies for temperature and ice volume reconstructions based on oxygen isotopes and Mg/Ca ratios in benthic foraminifera, this study aims to reconstruct deep ocean temperature by means of the clumped isotope thermometer (Δ_{47}). This proxy has the benefit that it does not rely on uncertainties like seawater chemistry and/or specific physiological characteristics of benthic foraminifera (Agterhuis et al., 2022).

Clumped isotopes are molecules which contain two or more rare isotopes (Eiler, 2007). These molecules have unique thermodynamic properties compared to molecules containing normal isotopes and therefore external effects on these isotope compositions can be neglected (Wang et al., 2004). Heavier isotopes create stronger bonds than light isotopes, where the energy difference between a heavy isotope substitution and a molecule with light isotope substitution is exactly twice as big following the rule of the mean (Affek, 2012; Eiler et al., 2007). However, the rule of the mean assumes there is no enthalpy of mixing the isotopes and a stochastic distribution occurs (Eiler et al., 2007). Therefore, only at high temperatures there will not be an advantage for chemical bonds to substitute two heavy isotopes and there is a preference for substation and bonding of heavy isotopes at lower temperatures (Affek, 2012; Eiler et al., 2007). The different clumped isotopes and their relationship with temperature are shown in figure 1.2, where generally heavier isotopes are more strongly dependent on temperature (Wang et al., 2004).

Figure 1.2 shows the different clumped isotopes, varying from Δ_{44} to Δ_{49}. Δ_{49} is the most dependent of temperature, but also the least abundant (Ghosh et al., 2006). Δ_{47} has a relatively high abundance and temperature dependence and is therefore commonly chosen for clumped isotope thermometry (Ghosh et al, 2006; Eiler et al., 2007). Equation 1.1 shows the calculation for the Δ_{47} value (Affek, 2012).

$$(1.1)\ \Delta_{47} = \left[\frac{R47}{2*R13*R18+2*R17*R18+R13*(R17)^2} - \frac{R46}{2*R18+2*R13*R17+(R17)^2} - \frac{R45}{R13+2*R17} + 1\right]*1000$$

- Where R47, R46, R45 are the ratios over mass 44
- Where R13, R17, R18 are the ratios over mass 44 following the stochastic abundance

Because clumped isotopes are only dependent on temperature and not on seawater chemistry and physiology of the species, clumped isotope thermometry gives an advantage over commonly used stable isotope ratio mass spectrometry (Agterhuis et al., 2022). Along with the Δ_{47} measurements, the separate $\delta^{18}O$ and $\delta^{13}C$ values can be obtained for additional research. The temperature can be derived directly because external factors do not need to be corrected and the biogenic and chemical seawater composition can be derived from $\delta^{18}O$ measurements (Hollis et al., 2019). However, clumped isotope thermometry also knows limitations. Clumped isotopes are not significantly abundant in nature and therefore large amounts of sample masses are needed to acquire adequate results (Affek, 2012; Hollis et al., 2019). Clumped isotope measurements can contain errors due to isotopic fractionations during sample preparation, sample purification and mass spectrometry (Huntington et al., 2009). Recrystallization, dissolution and diagenesis of calcite can also bias measurements (Hollis et al., 2019). Several different Δ_{47} temperature calibrations have been modified by laboratory specific methodology, adjusted to the instrumentation, ion corrections and standards. Results may therefore differ amongst several laboratories (Hollis et al., 2019).

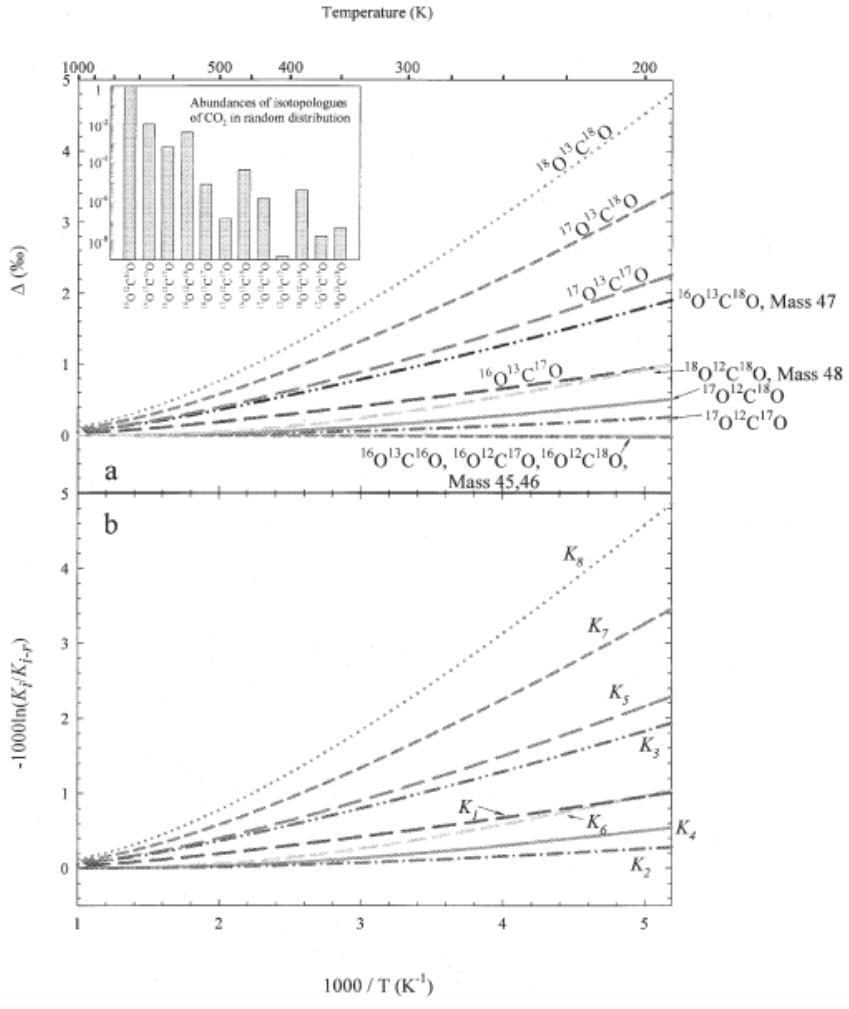

Figure 1.2: Relationship between temperature and abundance of the different clumped isotopes (Wang et al., 2004)

1.3 Research aim

The aim of this study is to reconstruct deep-sea temperatures at the Walvis Ridge ODP site 1263 by using clumped isotope thermometry of benthic foraminifera across the Eocene-Oligocene transition. Clumped isotopes provide a more accurate reconstruction of temperatures in comparison to conventional oxygen isotope and Mg/Ca thermometry and is independent of external factors. The results will be compared with companion MSc studies on the interval prior- and after the EOT and to previous estimates derived from oxygen isotope records, Mg/Ca ratios and TEX_{86} measurements. At last, the change in isotopic composition of the seawater will be determined by using the clumped isotope deep sea temperatures. This will determine the increase in size of the Antarctic ice sheet during the EOT.

Methods

2.1 Sampling location

The Walvis Ridge is an aseismic ridge west of the African coast, formed by a volcanic hot spot (Bordiga et al., 2015; O'Connor et al., 1990). It is a mountain chain that functions as a barrier between the Angola Basin in the north-west and the Cape Basin in the south-east (Alegret et al., 2007; Zachos et al., 2004).

Cores were taken from site 1263 (28° 31.98′S, 2° 46.77′E) during the Ocean Drilling Program (ODP) Leg 208. Leg 208 is located on the Walvis Ridge in the eastern South Atlantic (figure 2.1) and consists of six drill sites at various water depths (figure 2.2). This research is focused on Site 1263, which is considered to be the shallowest drill site of Leg 208 with a water depth of 2717m. The sediment of Site 1263 is subject to research because it covers the Cenozoic until the upper Paleogene and contains well preserved calcareous organisms, as it has been at least 1km above the Carbonate Compensation Depth (CCD) during the EOT (Peck et al., 2010).

The lithology of Site 1263 consists of nannofossil ooze, chalky nannofossil ooze, foraminifera-bearing nannofossil ooze and clay-bearing nannofossil ooze (Langton et al., 2016). Four adjacent holes at Site 1263 resulted in a composite depth record of 340m down, whereas the sample depths were converted to age by establishing an age model through magnetostratigraphy, biostratigraphy and astronomically tuned stable isotopes (Westerhold et al., 2015; Peck et al., 2010).

The interval between the late Eocene – early Oligocene (33.16 – 34.01 Ma) is chosen for this research. It covers the EOT and corresponds with a sample depth of 88.6 – 97.13 cm, acquired from Hole 1263B.

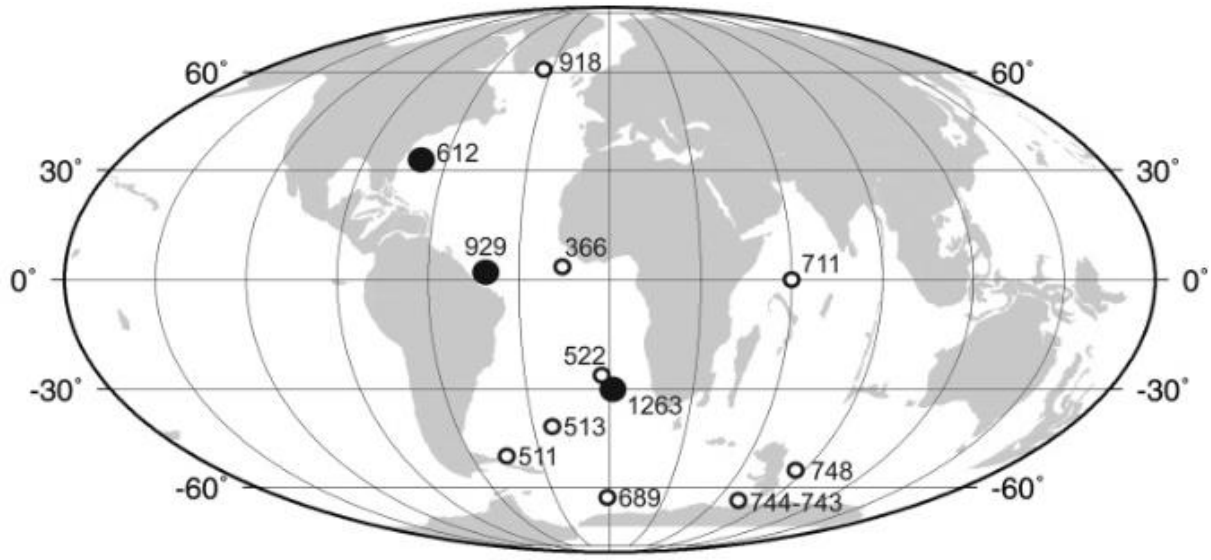

Figure 2.1: Location of the ODP 1263 drill site (Bordiga et al., 2017)

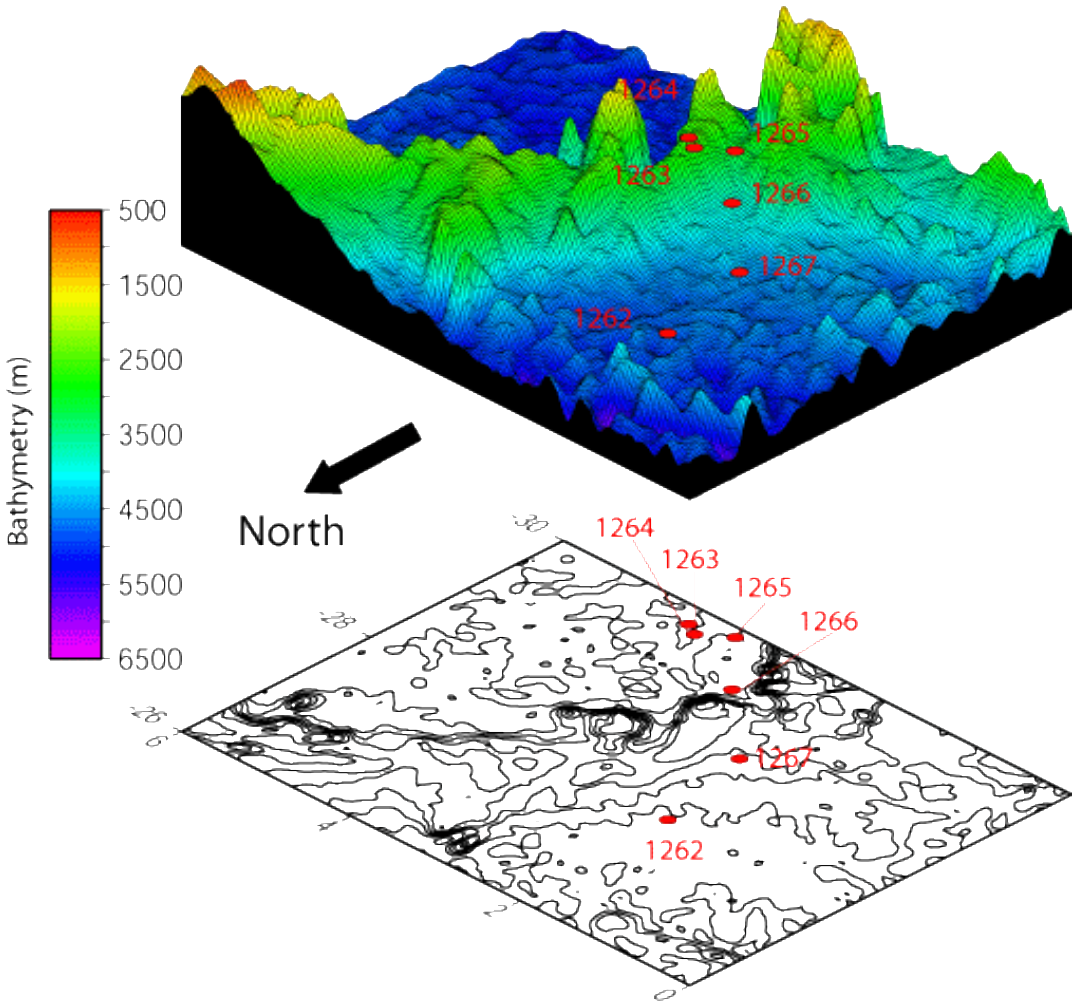

Figure 2.2: Bathymetric map of ODP leg 208 drill site locations (Zachos et al., 2004)

2.2 Sample preparation

The samples were freeze-dried and washed with tap water through sieves with >150, >63 and >38 µm fractions. The remaining sediment on the >150 µm sieve has been transferred to glass bowls by the use of DI water and left to dry in an oven at 40°C. After the samples were dried, they were transferred into small glass tubes and labelled.

The samples were then observed under the microscope and the benthic foraminifera were picked out. The species are defined according to the Holbourn, Henderson and MacLeod (2013) species definition. This research focused on the benthic *Oridorsalis umbonatus*, *Cibicoides havanensis* and *Cibicoides spp.* species, although other benthic species were also picked for possible other research. These benthic species were chosen because they can be directly compared to other EOT clumped- and $\delta^{18}O$ isotope records.

After separating the different species, the samples were cleaned to minimize the contamination in the different benthic species. The foraminifera were moisturized with DI water and crushed between two glass slides. The residue was transferred to Eppendorf tubes (0.5 mL) which were filled up with DI water. After removing the excess water, the tubes were put in an ultrasonic bath for one minute to detach the remaining sediments in the foraminifera, tapped to bring the materials into suspension and filled up with DI water by a pipet. The excess water was removed and put in the ultrasonic bath again, this process was repeated twice until the residue was transparent and contained no more sediment. The Eppendorf tubes were left open overnight for the residue to dry at normal temperatures.

2.3 Foraminifera description

The foraminifera *O. umbonatus*, *C. havanensis* and *C. spp.* were subject to research. The time and place of occurrence, as well as the characteristics will be discussed in the following section. The Appendix shows the definitions of the different foraminifera characteristics that are used.

O. umbonatus (figure 2.3) has a wide bathymetric distribution, it is found in the lower neritic to abyssal zone. The species first originated in the middle Paleocene and is still present this day (Holbourn et al., 2013). Tests of the *O. umbonatus* are compressed and lenticular, with a low trochospire. They are shaped subcircular to lobulate in outline and dissimilar biconvex in cross-section. The spiral side consists of radial sutures and the umbilical side consists of straight sutures. The aperture extends from the periphery until the closed umbilicus and is an interiomarginal slit (Holbourn et al., 2013).

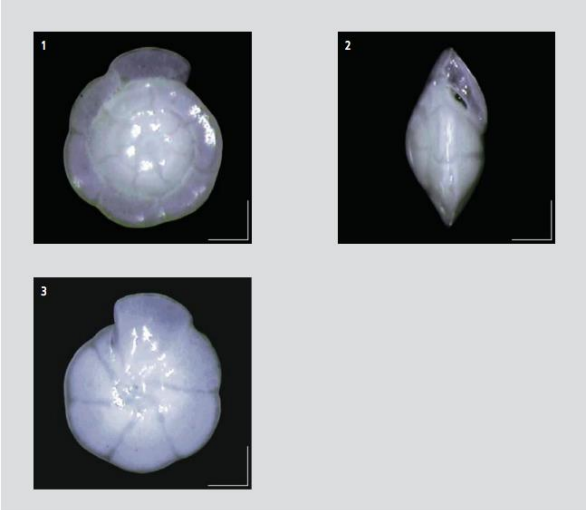

Figure 2.3: *Oridorsalis Umbonatus* photographed by Holbourn, Henderson and MacLeod, 2013.

C. havanensis (figure 2.4) is primarily found in the abyssal zone, but also occur in the middle bathyal zone. The species occurred from the Ypresian (Early Eocene) until Serravellian (Middle Miocene). Tests of the *C. havanensis* are large and dissimilar biconvex in cross-section. They consist of a partly evolute convex umbilical side and a strong evolute spiral side. The periphery is not perforated and subacute. Curvy sutures are found on the umbilical side and converges there towards the secondary shell growth area, strongly angled sutures are present at the spiral side. The aperture extends onto the spiral side and is a narrow equatorial slit (Holbourn et al., 2013).

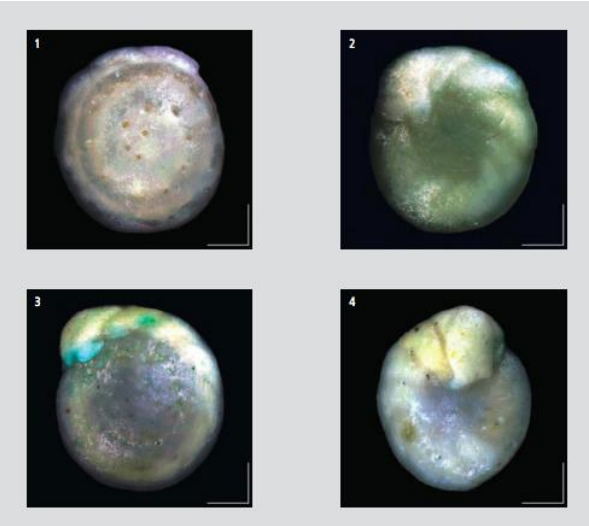

Figure 2.4: *Cibicoides havanensis*, photographed by Holbourn, Henderson and MacLeod, 2013.

C. praemundulus (figure 2.5) is found in the bathyal to abyssal zone. The species occurred from the Ypresian (Early Eocene) until the Aquitanian (Early Miocene). Tests of the *C. praemundulus* are subcircular in outline and nearly biconvex in cross-section, with a biumbonate trochosphere. Both the umbilical as the spiral side are convex. The periphery is not perforated and subacute. The sutures are curvy and present on both sides. The aperture extends onto the spiral side and is a narrow equatorial slit (Holbourn et al., 2013).

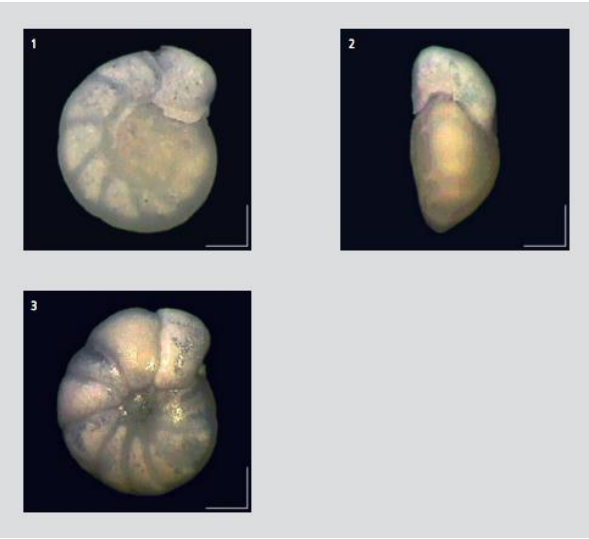

Figure 2.5: *Cibicoides praemundulus*, photographed by Holbourn, Henderson and MacLeod, 2013.

2.4 Instrumental setup

Stable isotope mass spectrometry measurements of the benthic foraminifera species were carried out at the GeoLab of the Utrecht University. The *Thermo Scientific Kiel IV Carbonate Device* in combination with *Thermo Scientific 253 Plus 10 kV* was used for these measurements. Both samples and standards are weighed in before starting a run. The standards consist of ETH-1, ETH-2, ETH-3, MERCK and IAEA-C2 and the accepted values are shown in table 2.1. The samples used for measurements varied between 70-90 µg. Runs consisted of 46 samples, of which 22 were benthic foraminifera samples and 24 were standards (Kocken et al., 2019). The *Thermo Scientific Kiel IV Carbonate Device* (figure 2.6) was loaded with the samples and the residue of the samples was dissolved with 102-105% phosphoric acid and a vacuum pump at 70 °C. This resulted in sublimation of the solid materials, and the release of CO_2 gas. The CO_2 gas was captured in a liquid nitrogen trap with a temperature of -196 °C. Heating the liquid nitrogen trap to 100 °C resulted into the movement of the CO_2 through the *Porapak-Q Mesh* trap, which had a temperature of -50 °C. The CO_2 was transferred and captured in a second liquid nitrogen trap with a temperature of -196 °C. After capturing, the CO_2 was transferred to the mass spectrometer *Thermo Scientific 253 Plus 10 kV* for stable isotope ratio measurements. This mass spectrometer contained Faraday cups for m/z 44, 45, 46, 47, 47.5, 48 and 49.

Standard	**$\delta^{13}C$ (‰ VPDB)**	**$\delta^{18}O$ (‰ VPDB)**	**Δ47 (I-CDES)**
Reference gas	-4.670	-2.820	
ETH-1	1.988 ±0.184	-2.363 ±0.512	0.200 ±0.045
ETH-2	-10.150 ±0.054	-18.819 ±0.130	0.206 ±0.048
ETH-3	1.711 ±0.053	-1.780 ±0.103	0.613 ±0.050
IAEA-C2	-8.112 ±0.041	-9.044 ±0.059	0.634 ±0.061
Merck	-41.848 ±0.246	-15.728 ±0.220	0.516 ±0.046

Table 2.1: Values for standards.

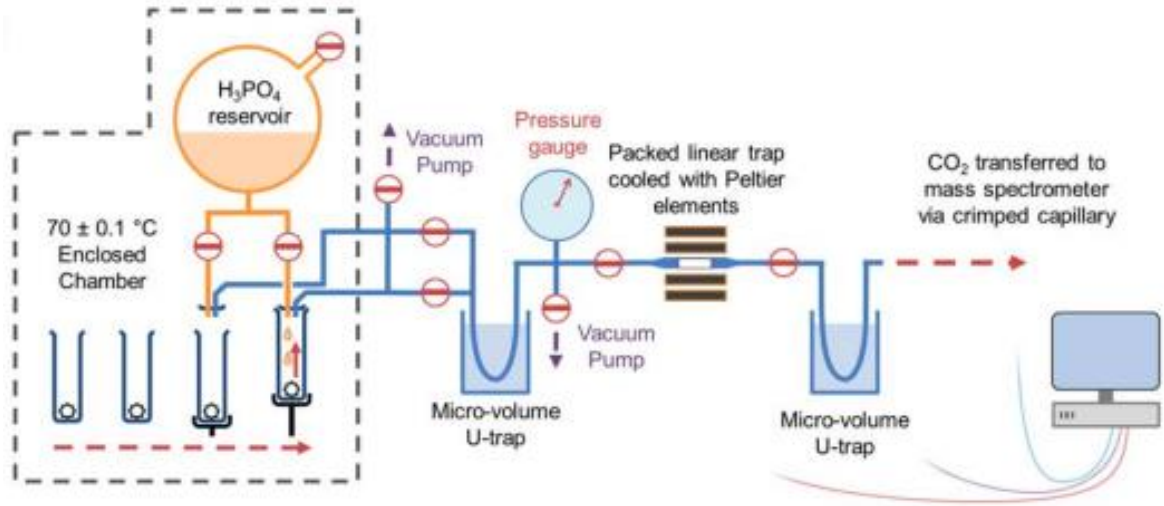

Figure 2.6: Schematic overview of the instrumental setup of the *Thermo Scientific KIEL IV Carbonate Device* (Spencer and Kim, 2019).

2.5 Complications and corrections

During measurements of the Δ47 (I-CDES) clumped isotopes, complications may occur. Because the mass spectrometer consists of stainless-steel capillaries, isotope redistribution reactions may occur (Passey et al., 2010). This means isotope exchange will occur and results in an alteration from Δ47 to Δ44. However, the stainless-steel capillaries at the GeoLab of the Utrecht University are not affected. The isotope redistribution reactions for this research can therefore be neglected.

Heating of CO_2 to 100 °C results in a more stochastic distribution of isotopes in the ion source, affecting the Δ47 (I-CDES) clumped isotope values (Huntington et al., 2009; He et al., 2012). This can be solved by lowering the pressure of the CO_2 and the residence time of CO_2 in the source (Huntington et al., 2009).

When the CO_2 is transferred into the mass spectrometer, a baseline signal is being measured in the source. This baseline is determined by secondary electrons entering the Faraday cup and by widening of the m/z 44 ion beam (He et al., 2012). Secondary electrons of the m/z 44 ion beam collide with the flight tube after the ion beam leaves the magnetic field of the mass spectrometer (He et al., 2012). These secondary electrons originate by scattering and energy-loss processes (Schou, 1980). The collisions result in a negative baseline and affect the baseline values of m/z 47 ion beams (He et al., 2012). Scattering and the repulsive force between positive ions and negative electrons result in widening of the ion beam (He et al., 2012). Because of the widening, m/z 44 molecules can end up in the m/z 47 Faraday cup, resulting in baseline signal asymmetry in this cup (He et al., 2012). A background scan before starting a run was therefore be done to correct for these baseline values. The reference gas was scanned for 44 m/z at 5V, 10V, 15V, 20V and 25V and subtracted from the final 47 m/z values to correct for the m/z 47 values (Meckler et al., 2014). Because Δ_{47} (I-CDES) clumped isotopes are less often found than other stable isotopes, a larger sample size is needed to achieve mass spectrometer stability (Huntington et al., 2009; He et al., 2012).

After correcting the baseline, the total raw Δ_{47} bulk isotope composition of the standards was measured for inter-laboratory comparison. The bulk isotope composition was calculated based on previous $\delta^{18}O$ and $\delta^{13}C$ values of ETH-1, ETH-2 and ETH-3 (Bernasconi et al., 2021). The measured Δ_{47} values of the samples were converted to the I-CDES90°C (InterCarbon-dioxide equilibrium scale) absolute reference frame with the empirical transfer function (ETF; Equation 2.1; Bernasconi et al., 2021).

(2.1) $$\Delta_{47\,(\text{I-CDES90°C})} = a * \Delta_{47\text{raw}} + b$$

- Where a is the regression slope and b is the intercept
- Where $\Delta_{47\text{raw}}$ are the measured values of the samples
- Where $\Delta_{47\,(\text{I-CDES90°C})}$ are the I-CDES90°C absolute reference frame values

2.6 Equations

The age model is derived by data of the Peck et al. (2010) paper. Two tie points were used to derive a linear equation to convert sample depth to age. The linear equation that was derived is shown in equation 2.2.

(2.2) Age (Ma) = 0.1 * sample depth (mbsf) + 24.3

For calculating the absolute temperature by the means of Δ47 (I-CDES) values, two different temperature calibrations were used. Firstly, the temperature was derived from the Meinicke et al. (2021) calibration method (equation 2.3).

(2.3) Δ_{47} (I-CDES) = (0.0397 ±0.0011) x 10^6 / T^2 + (0.1518 ± 0.0128)

- Where T is the temperature in Kelvin
- Where Δ47 is the mean Δ47 values per singular or multiple measurements

Secondly, the temperature was derived from the Peral et al. (2022) calibration method (equation 2.4).

(2.4) $T\,(K) = \sqrt{\frac{A*10^3}{\Delta_{47\,(I\_CDES)} - B}} - 273\,(K)$

- Where A = 37 and B = 0.181
- Where T is the temperature in Kelvin
- Where Δ_{47} is the mean Δ_{47} values per singular or multiple measurements

To calculate the temperature effect of the $\delta^{18}O$, the $\delta^{18}O_{sw}$ according to the Δ47 (I-CDES) derived temperatures is calculated. The Marchitto et al. (2014) temperature calibration is used (equation 2.5). The measured oxygen- and carbon isotopes have been corrected for the *C. spp*. The correction values are shown in table 2.2.

(2.5) $T = \frac{0{,}245 - \sqrt{0{,}045461 + 0{,}0044(D18O - Dsw)}}{0{,}0022}$

- Where T is the temperature in degrees Celsius (°C)

Species	Isotope	Correction factor
Oridorsalis	$\delta^{18}O$	Cib = Orid – 0.28
Oridorsalis	$\delta^{13}C$	Cib = Orid + 0.72

Table 2.2: Corrected values for *Oridorsalis umbonatus*

2.7 Uncertainties

Numerous uncertainties appeared that affected the final Δ_{47} temperatures. Firstly, measurements may be influenced by lab activities or analytical uncertainties. Lab activities are done by hand and checked numerous times to minimize error propagations, analytical uncertainties are minimized by applying corrections.

Secondly, the baseline values might not be adjusted properly. Errors that occur by baseline adjustments have a large influence on the measurements (Kocken et al., 2019). This can be prevented by adding in an extra standard and change the ratio of the standards used for a run to minimize errors (Kocken et al., 2019).

Last, the temperature calibrations that are used are still subject to research. The Meinicke et al. (2020) calibration was derived from a Matlab script that followed the equations of Huntington et al. (2009). The Peral et al., 2022 temperature calibration was derived from a recomputation of multi-foraminiferal species of Peral et al., 2018 and modified to the newest Δ_{47} methodological advancements (Peral et al., 2022). Both the temperature calibrations have been used to clarify the difference.

Results

3.1 Derived $\delta^{18}O$ and $\delta^{13}C$ values and interval selection

A total of five bins were realized (figure 3.1). Two bins are set in the early Oligocene, consisting of 33.28 Ma (33.16-33.39 Ma) and 33.53 Ma (33.42-33.61 Ma). One bin represents the EOT and consists of 33.67 Ma (33.62-33.70 Ma). Two bins are set in the late Eocene, consisting of 33.79 Ma (33.72-33.86 Ma) and 33.95 Ma (33.88-34.01 Ma).

The age model is derived from the Peck et al., 2010 paper. The sample depths (mbsf) from this research are converted to ages using a linear regression line, derived from comparing the sample depths (mbsf) to ages of Peck et al., 2010. The tie points used for this linear regression line are shown in table 3.1 and equation 2.2 is used for the calibration.

Depth	**Age**
86	32.9
96	33.9

Table 3.1: Tie points of Peck et al., 2010 used for the linear age calibration

Figure 3.1 show each of the five bins with the total benthic $\delta^{18}O$ and $\delta^{13}C$ values, which are derived from measurements on the *O. umbonatus*, *C. havanensis* and *C. spp*. The benthic $\delta^{18}O$ and $\delta^{13}C$ values derived from the *O. umbonatus* are corrected to the *C. spp*. The benthic $\delta^{18}O$ records show almost steady values with a slight change during the late Eocene (bin four and five) and an increase of ~1.5‰ to ~2.3‰ of the $\delta^{18}O$ values during the EOT, with only slight changes during the early Oligocene. The benthic $\delta^{13}C$ records show an increase of ~1.2‰ to ~1.7‰ during the late Eocene until the early Oligocene.

A

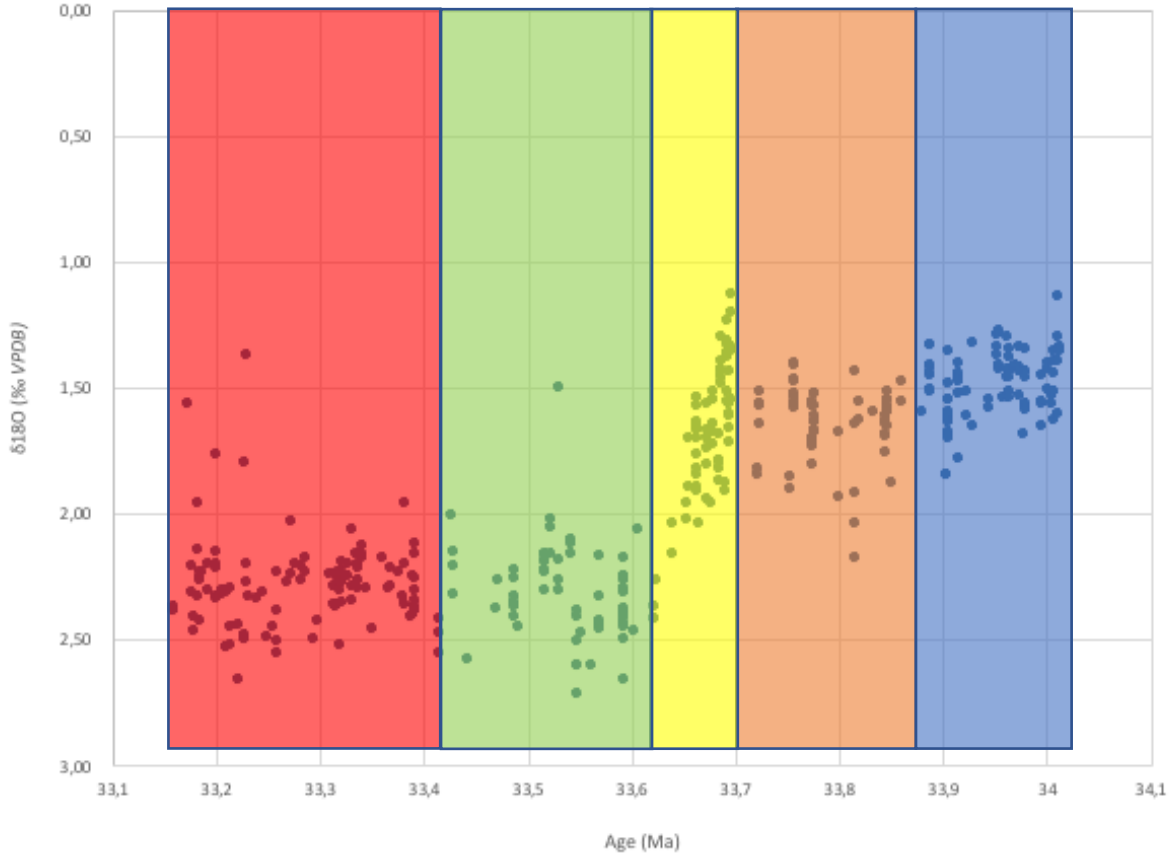

B

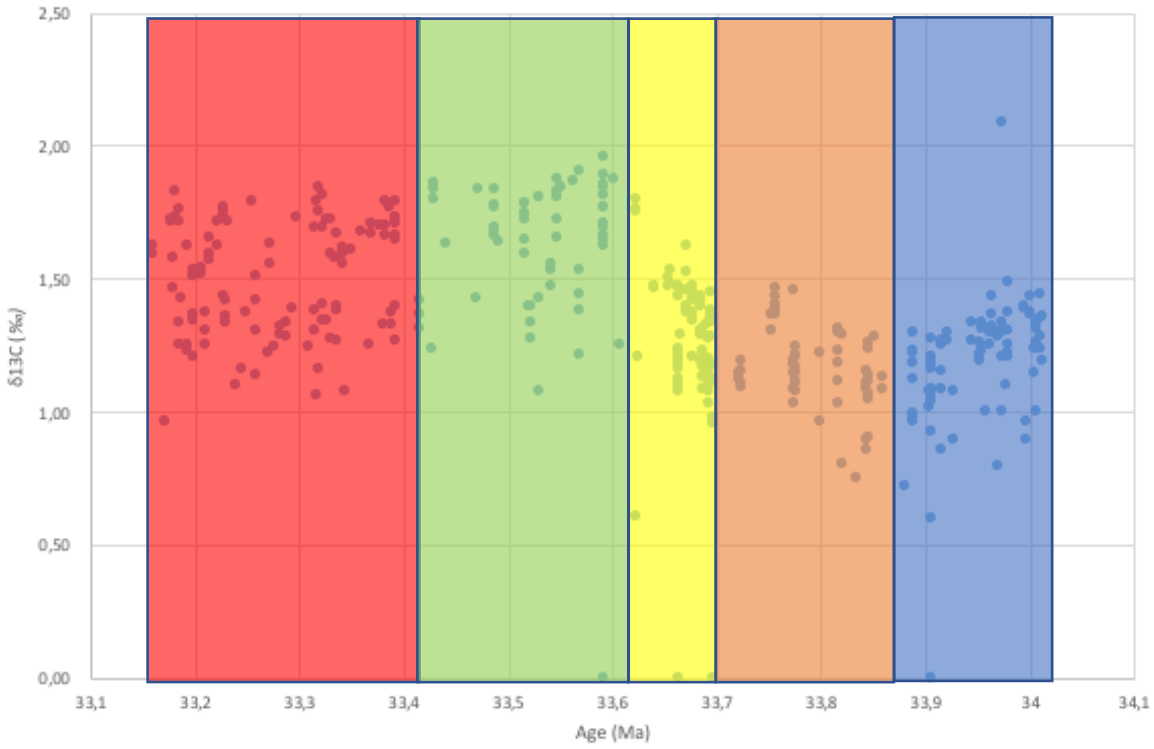

Figure 3.1: Overview of the $\delta^{18}O$ ‰ VPDB record and $\delta^{13}C$ ‰ record with the five bins.

3.2 General results

The measurements on the *Oridorsalis umbonatus, Cibicidoides havanensis* and *Cibicidoides spp*. were used to calculate the Δ47 (I-CDES) values, $\delta^{18}O$ (‰ VPDB) values and corresponding temperatures (°C). The results per bin are shown in figure 3.2, whereas the age (Ma) is calibrated from the linear regression model derived from Peck et al., 2010. The average Δ47 values were 0.653 ±0.01 for 33,28 Ma, 0.650 ±0.01 for the early Oligocene (33.53 Ma), 0.650 ±0.009 for the EOT (33.67 Ma), 0.664 ±0.01 for the late Eocene (33.79 Ma) and 0.652 ±0.009 for 33.95 Ma. The vertical error bars correspond with the 95% confidence levels (figure 3.1A). The standard deviations of the control groups are shown in table 3.2, whereas the Δ47 standard deviation of ETH-3 is 0.050‰. This corresponds with the derived standard deviations of the measurements of this research.

Figure 3.1B shows the general trend of $\delta^{18}O$ over the timeseries, combined with the average $\delta^{18}O$ per bin. The trend is almost stable, with an increase of $\delta^{18}O$ during the EOT (33.7 Ma). This trend corresponds with previous studies (Cramer et al., 2011; Petersen & Schrag, 2015)

The temperatures as calculated from Δ47 (I-CDES) and $\delta^{18}O$ (‰ VPDB) values are shown in figure 3.1C. For the Δ47 (I-CDES) calculated temperatures, the Meinicke et al., 2021 calibration (equation 2.3) shows 8.43 ±2.78 °C for 33.28 Ma, 9.22 ±2.81 °C for 33.53 Ma, 9.25 ±2.44 °C for the EOT (33.67 Ma), 5.39 ±2.75 °C for 33.79 Ma and 8.55 ±2.61 °C for 33.95 Ma. The Δ47 (I-CDES) temperatures are also calculated by using the Peral et al., 2022 calibration (equation 2.4). This resulted in a temperature of 7.13 ±2.93 °C for 33.28 Ma, 7.96 ±2.97 °C for 33.53 Ma, 8.00 ±2.58 °C for the EOT (33.67 Ma), 3.91 ±2.89 °C for 33.79 Ma and 7.26 ±2.75 °C for 33.95 Ma. The average calculated temperatures calculated by the Peral et al., 2022 calibration are significantly lower than the average calculated temperatures by Meinicke et al., 2021. However, the same general trend can be seen. This general trend partly correlates with the $\delta^{18}O$ (‰ VPDB) derived temperatures, calculated using the Marchitto et al., 2014 calibration (equation 2.5), assuming that the $\delta^{18}O$ (‰ VPDB) seawater varies between -0.1 ‰ VSMOW and -0.9 ‰ VSMOW (Cramer et al., 2011). The Marchitto et al., 2014 calibration results in a temperature of 3.88 °C for 33.28 Ma, 2.87 °C for 33.53 Ma, 4.74 °C for the EOT (33.67 Ma), 4.01 °C for 33.79 Ma and 3.83 °C for 33.95 Ma. The $\delta^{18}O$ (‰ VPDB) temperature calibration indicates an increase in temperature during the late Eocene (bin 4), while the Δ47 (I-CDES) temperature calibrations indicate an decrease in temperature during the late Eocene. However, both $\delta^{18}O$ and Δ47 temperature calibrations show an increase of temperature during the EOT with a decrease during the early Oligocene.

Figure 3.1D shows the $\delta^{18}Osw$ (‰ VPDB) values, as calculated by using equation 2.5. The Δ47 temperature is calculated by using the Meinicke et al., 2021 calibration (equation 2.3). The $\delta^{18}Osw$ (‰ VPDB) values are 0.61‰ for 33.28 Ma, 0.84‰ for 33.53 Ma, 0.19 for the EOT (33.67 Ma), -0.73‰ for 33.79 Ma and -0.17‰ for 33.95 Ma. During the early Oligocene (33.79 Ma) a value of -0.73‰ is reached, which is close to the $\delta^{18}Osw$ (‰ VPDB) values of the last glacial maximum (LGM; Schrag et al., 2002).

	Δ47	**$\delta^{18}O$**	**$\delta^{13}C$**
ETH-1 (N=19)	0.045	0.141	0.070
ETH-2 (N=19)	0.048	0.130	0.054
ETH-3 (N=95)	0.050	0.103	0.053

Table 3.2: Standard deviations of the ETH control groups

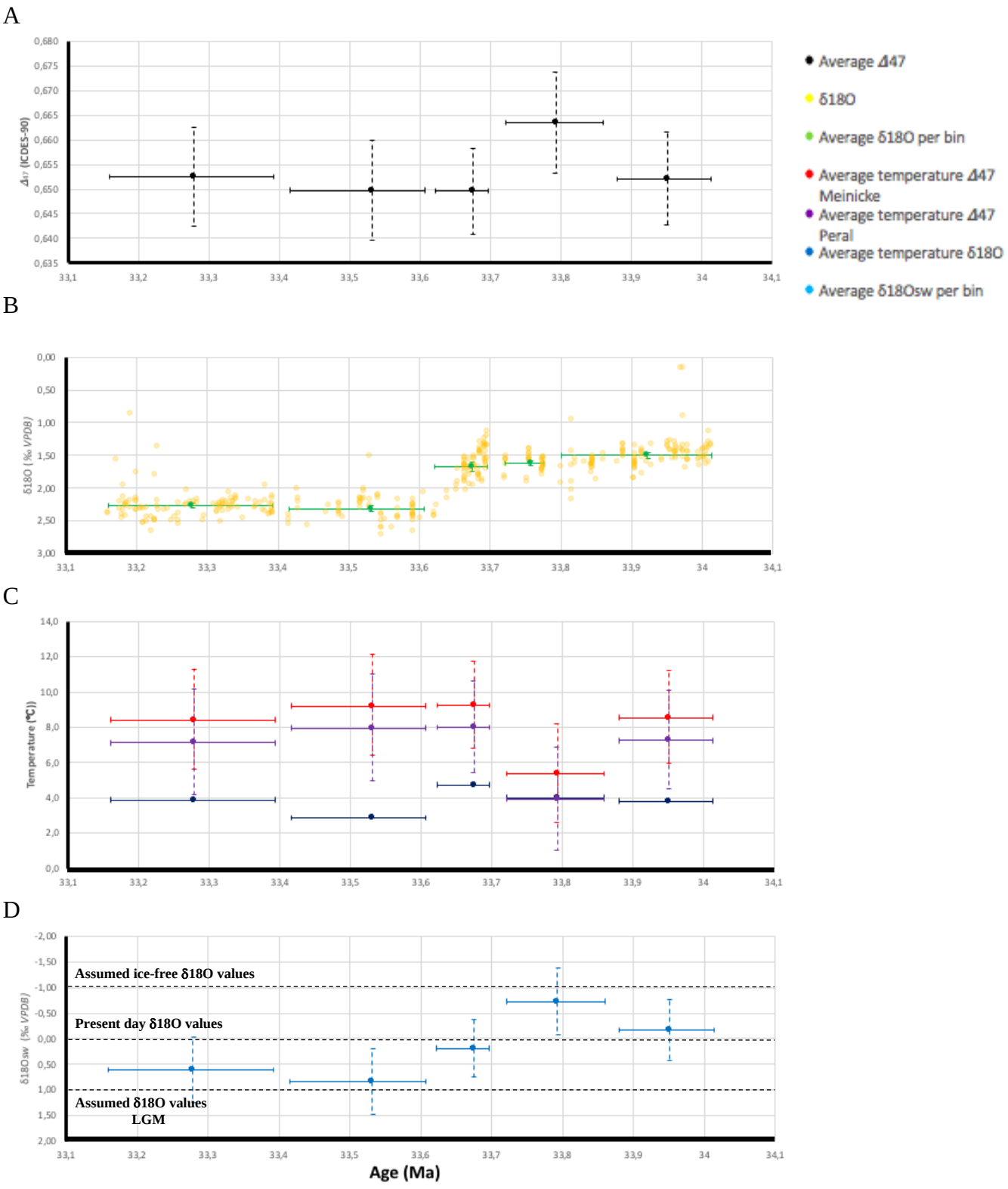

Figure 3.2: Overview of stable isotope records and calculated temperatures. Horizontal error bars represent the temporal range, vertical error bars indicate the 95% confidence level. A: Mean Δ47 values per bin. B: δ18O record of sample in orange, mean $\delta^{18}O$ values per bin in green. C: In red the mean temperature calculated for Δ47 per bin using the Meinicke et al., 2021 calibration. In purple the mean temperature calculated for Δ47 per bin using the Peral et al., 2022 calibration. In dark blue the mean temperature calculated for $\delta^{18}O$ using the Marchitto et al., 2014 calibration, assuming $\delta^{18}Osw$ varies between -0,1 ‰ VSMOW and -0,9 ‰ VSMOW (Cramer et al., 2011). D: Calculated $\delta^{18}O$ values of the seawater, using the Marchitto et al., 2014 calibration. Horizontal lines indicate previous assumptions of $\delta^{18}O$ and present-day values (Schrag et al., 2002**)**.

3.3 Average temperature reconstruction along the timeseries

The temperature records are calculated with a moving average (figure 3.3). The moving window of the averages consist of 40 data points each, for 395 data points in total. The temperature is derived from the Δ47 Meinicke et al., 2021 calibration and consist of all temperature measurements. The clumped isotope temperatures show a gradual decrease of temperature in the late Eocene, with a significant decrease in temperature of ~3.5 °C (7.04°C – 3.5 °C) at the beginning of the EOT. The EOT (marked in blue; Peck et al., 2010) is characterized by a temperature increase of ~7 °C (3.5 °C - 10.45 °C). The temperature lowers slightly during the early Oligocene and increases again around ~33.75 Ma.

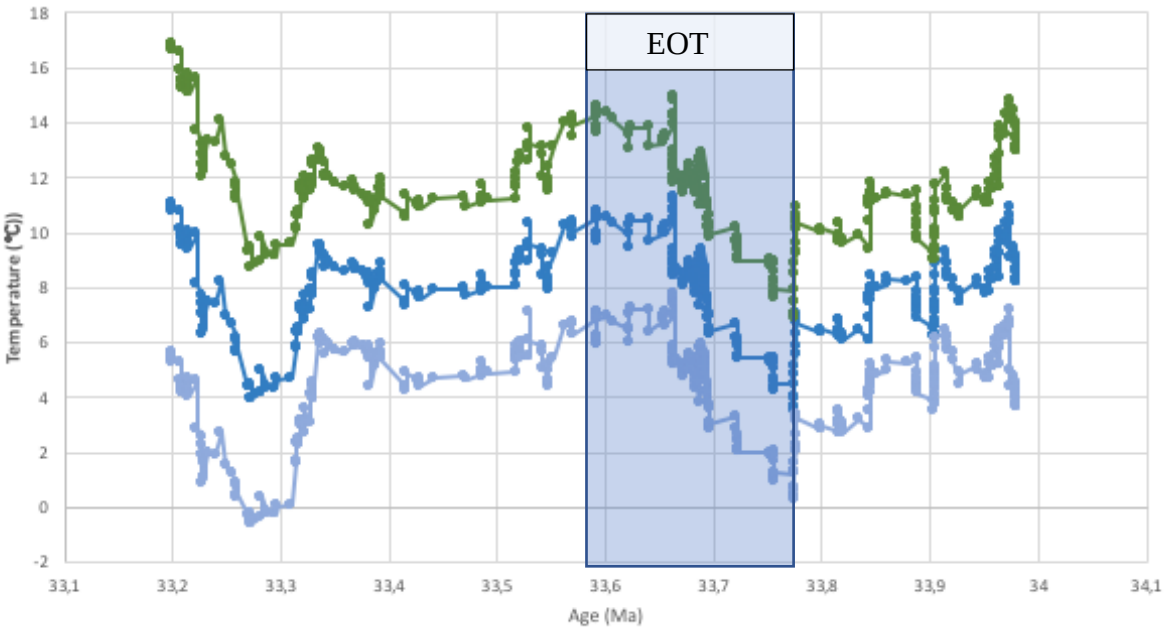

Figure 3.3: Temperature records calculated with a moving average, the temperature is derived from the Meinecke et al., 2021 calibration. Dark blue represents the moving average of the mean temperatures, light blue and green lines represent respectively the moving average of the minimum and maximum temperature calculated by the 95% confidence interval.

Discussion:

4.1 Deep ocean water temperatures derived from Δ47, $\delta^{18}O$ and Mg/Ca

Figure 4.1 shows a comparison between temperatures derived from Δ_{47}, $\delta^{18}O$ and Mg/Ca data from Cramer et al., 2011. Two calibrations were used to derive the Mg/Ca based temperatures. One is based on the Lear et al., 2010 calibration, the other is based on the Rathmann et al., 2004 calibration. Both the Mg/Ca calibrations are based on *O. umbonatus* and show a significant difference in temperature (±1°C; Cramer et al., 2011). The reason for the offset between the two Mg/Ca temperature calibrations are unclear, although the same general trend can be seen (Cramer et al., 2011).

Two Δ_{47} temperature calibrations were used to derive temperatures. Figure 4.1A shows the Meinicke et al., 2021 calibration compared to $\delta^{18}O$ and Mg/Ca derived temperatures, figure 4.1B shows the comparison of the Peral et al., 2022 calibration. Both calibrations show a significant temperature offset between Δ_{47}, $\delta^{18}O$ and Mg/Ca. The offset between Δ_{47} and $\delta^{18}O$ temperatures can be explained by the dependence of $\delta^{18}O$ on seawater chemistry, physiology of benthic foraminifera and pH of the seawater (Agterhuis et al., 2022). The $\delta^{18}O$ temperature calibration of Marchitto et al., 2014 is calculated by estimating the $\delta^{18}O_{sw}$ composition over time. This can result in biased measurements because $\delta^{18}O_{sw}$ is largely dependent on salinity, which varies spatially in the ocean (Zachos et al., 1994; Rohling, 2013), and changes in the cryosphere (Cramer et al., 2009). It is assumed that the foraminifera are formed in isotopic equilibrium with the seawater (Hollis et al., 2019). However, the physiology and ecology of the foraminifera are not considered, resulting in biased temperature reconstructions (Hollis et al., 2019). The offset of $\delta^{18}O$ temperature can also be explained by the pH effect on foraminiferal $\delta^{18}O$ (Zeebe et al., 2001). The decline of seawater pH results in an increase of foraminiferal $\delta^{18}O$ (Uchikawa & Zeebe, 2010). The pH effect on benthic foraminifera have been poorly studied (Uchikawa & Zeebe, 2010), so the effect of pH on $\delta^{18}O$ of this research is unknown. It can therefore be concluded that the assumptions of $\delta^{18}O$ temperature calibrations are inaccurate.

When comparing the Δ_{47} temperatures according to Meinicke et al., 2021 and Peral et al., 2022 calibrations to the Mg/Ca temperatures of Cramer et al., 2011, a correlation between the Peral et al., 2022 temperature calibration and the Mg/Ca temperature calibration of Rathmann et al., 2004 can be seen. The Δ_{47} temperature of Peral et al., 2022 mostly fall within the 95% confidence interval of Rathmann et al., 2004 (Figure 4.1B). Generally, a correlation between Mg/Ca temperature trends and Δ_{47} temperature trends is seen (Evans et al., 2018). However, the general trend of the Mg/Ca temperatures and Δ_{47} temperatures do not correspond. The cooling at the end of the Eocene (bin 1 and 2) is not visible in the Mg/Ca temperature of Cramer et al., 2011. This means that the Mg/Ca trend is subject to incorrect assumptions and uncertainties as well.

The offset between Δ_{47}- and Mg/Ca derived temperatures can be explained by different factors. Firstly, significant fluctuations of Mg/Ca occur in the seawater over million-year timescales (Evans and Müller, 2012). This results in inaccurate Mg/Ca-derived temperatures and the Mg/Ca values need to be corrected before deriving temperatures (Evans and Müller, 2012). Secondly, the Mg/Ca dataset reflects a larger uncertainty since the record is based on different sites, the dataset is not continuously sampled and it consists of breaks in sequence

boundaries (Cramer et al., 2011). Thirdly, the calibrations used in Cramer et al., 2011 show a difference in temperature sensitivity for the different benthic foraminifera. This is caused by differences in exponent H of the Mg/Ca equations used by Cramer et al., 2011. Exponent H is dependent of $\delta^{18}O_{sw}$, which varied significantly over time (Cramer et al., 2011). Lastly, benthic foraminifera can be subject to diagenetic alteration, which affect the preservation (Pearson et al., 2001). It can be therefore concluded that the Mg/Ca temperatures are highly uncertain.

A

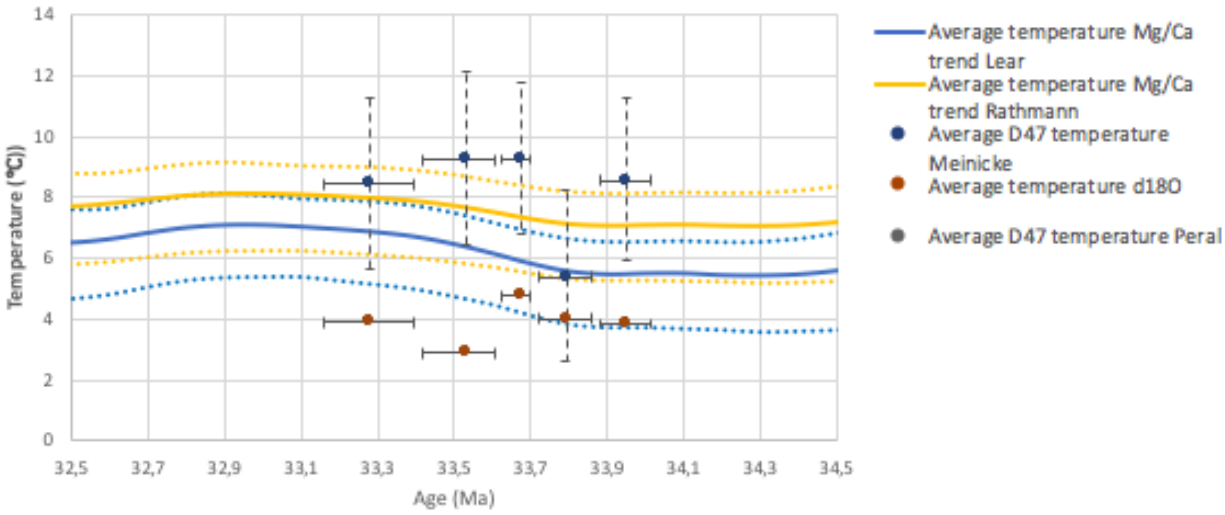

B

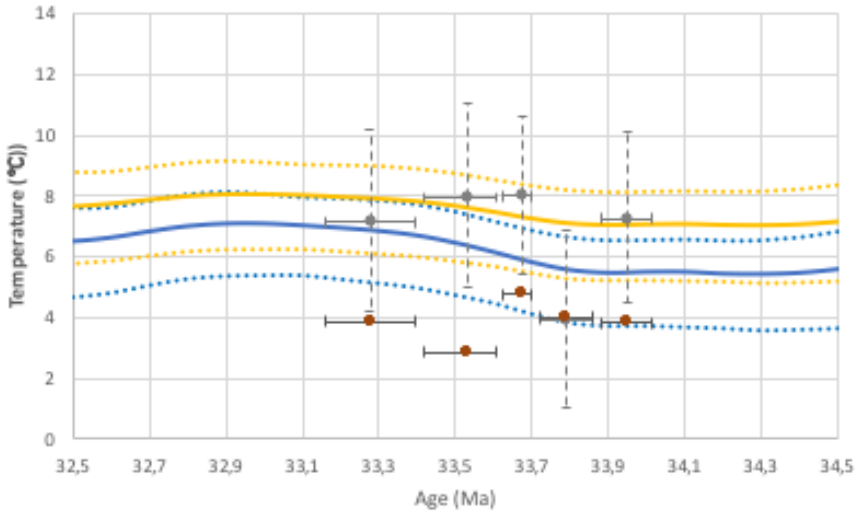

Figure 4.1: Mean Δ47 and $\delta^{18}O$ temperatures from this research compared to Mg/Ca temperature calculations from Cramer et al., 2011. The temperature calibration of Lear, Mawbey and Rosenthal, 2010, is shown in blue. The temperature calibration of Rathmann et al., 2004, is shown in yellow. The dotted lines indicate the 95% confidence interval. A: Comparison of mean Δ47 temperatures derived by Meinicke et al., 2021 calibration. B: Comparison of mean Δ47 temperatures derived by Peral et al., 2022 calibration.

4.2 $\delta^{18}O$ seawater composition derived from Δ47 and Mg/Ca

The average $\delta^{18}O_{sw}$ has been calculated with the derived Δ_{47} temperatures (equation 2.5) from this research and compared to the derived Mg/Ca $\delta^{18}O_{sw}$ values of Cramer et al., 2011 in figure 4.2. The $\delta^{18}O_{sw}$ derived from Δ_{47} temperatures have a benefit over $\delta^{18}O_{sw}$ derived by $\delta^{18}O$ since it is independent of temperature, seawater chemistry and specific characteristics of benthic foraminifera (Agterhuis et al., 2022).

The Mg/Ca $\delta^{18}O_{sw}$ trend correlates with the Δ_{47} $\delta^{18}O_{sw}$, although the $\delta^{18}O_{sw}$ at ±33,95 Ma deviates from the general trend. Although, the Δ_{47} $\delta^{18}O_{sw}$ values show generally significant lower values than the Mg/Ca derived $\delta^{18}O_{sw}$ values. The significant difference in values can be explained by the fact that the Mg/Ca record is sampled at different sites and because of the pH effect on the $\delta^{18}O$ of benthic foraminifera, which is discussed in section 4.1. Since the pH effect on benthic foraminifera is poorly studied (Uchikawa and Zeebe, 2010), this research did not include the pH effect and focused on the general trends instead. Since the temperature derived by Δ_{47} is independent of the assumptions made in section 4.1 for Mg/Ca temperature reconstructions, the $\delta^{18}O_{sw}$ values derived by Δ_{47} temperatures are more plausible to be correct.

A general cooling trend occurred globally from the Early Eocene Climatic Optimum (EECO), where the world was ice-free according to warm high latitude sea surface temperatures (Bijl et al., 2009; Schrag et al., 2002). Despite this significant cooling over time, $\delta^{18}O_{sw}$ values from this research reach values during the late Eocene (Bin 4; 33,79 Ma) close to the assumed ice-free values. Bin 4 corresponds with the lowest temperature derived by Δ_{47} in this research. The low deep-sea temperature in combination with the low $\delta^{18}O_{sw}$ values show a mismatch with previously assumed theories. The warmest deep-sea temperatures (i.e. 33,28 Ma and 33,53 Ma) show $\delta^{18}O_{sw}$ values close to the LGM. Therefore, it can be assumed that the formation of ice sheets is independent of the global temperature and the world was not entirely ice-free during the Eocene (Miller et al., 2005; Agterhuis et al., 2022).

The presence of continental ice sheets during the Eocene has been a major question before. According to the $\delta^{18}O_{sw}$ values based on Δ_{47} temperatures of this research and results of previous studies, it can be assumed that continental ice sheets were already present during the cool Eocene greenhouse and extended in size during the EOT (Ladant et al., 2014; Scher et al., 2011). This is supported by the presence of Ice Rafted Debris (IRD) in marine sediment samples from the middle Eocene onwards (Scher et al., 2011; Tripati & Darby, 2018). The extent of the global ice sheets was estimated equivalent to 15 to 40m sea level change during the middle to late Eocene and grew during the EOT equivalent to 50-60m sea level change (Miller et al., 2020). Fluctuations in $\delta^{18}O_{sw}$ are therefore not just dependent on the extent of ice sheets and must be affected by other factors as well.

The formation and melt of ice sheets during the Eocene affected the salinity of the seawater (Lynch-Stieglitz et al., 1999). The relationship between salinity and $\delta^{18}O_{sw}$ differs globally, saline deep waters formed easier at lower latitudes resulting in spatial differences of $\delta^{18}O_{sw}$ values (Lynch-Stieglitz et al., 1999; Lunt et al., 2010). This is most likely to be the main factor of $\delta^{18}O_{sw}$ fluctuations in this research and will be discussed more in depth in section 4.4.

Another factor for the $\delta^{18}O_{sw}$ fluctuations is the subsequent storage of ^{16}O in continental aquifers, which may have shifted the $\delta^{18}O_{sw}$ towards more positive values during the EOT (Sames et al., 2020). This process is called aquifer-eustasy and results in short-term sea-level fluctuations, especially during warm periods (Wendler et al., 2016; Sames et al., 2020).

Seafloor spreading rates can also be a factor that influences the $\delta^{18}O_{sw}$ composition. The oceanic crust has a constant isotopic composition, but releases ^{18}O to the seawater during high-temperature ocean crust-seawater reactions (Wallman, 2001). This process commonly occurs at mid-oceanic ridges but can also be applicable to the Walvis Ridge, since it is formed by a volcanic hot spot (Wallman, 2001; Bordiga et al., 2015). Seafloor spreading was likely to increase during the early Cenozoic, resulting in more release of ^{18}O to the seawater and thus affecting the $\delta^{18}O_{sw}$ compositions (Conrad & Lithgow-Bertelloni, 2007; Wallman, 2001).

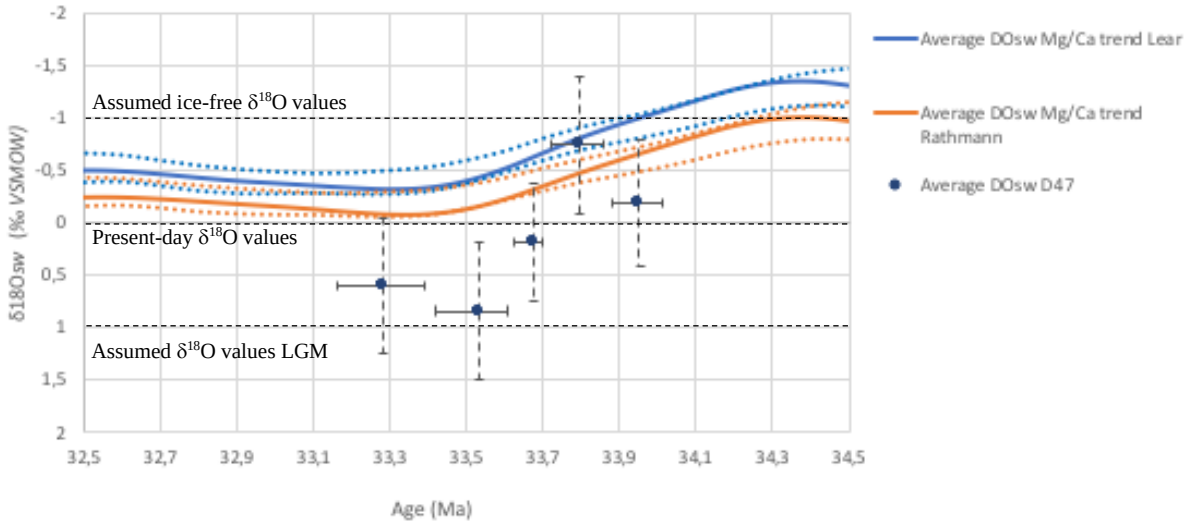

Figure 4.2: Mean calculated $\delta^{18}O$ seawater values from this research derived by $\Delta 47$ compared to Mg/Ca $\delta^{18}O$ seawater calculations from Cramer et al., 2011. The calibration of Lear, Mawbey and Rosenthal, 2010, is shown in blue. The temperature calibration of Rathmann et al., 2004, is shown in orange. The dotted lines indicate the 95% confidence interval.

4.3 Sea surface temperatures compared to deep ocean temperatures

A comparison between TEX_{86} reconstructed temperatures and Δ_{47} temperature is shown in figure 4.3. A significant TEX_{86} sea surface temperature (SST) increase during the EOT is seen for the Southern Atlantic Ocean (ODP site 925/929) and the Cayman Rise (ODP site 998). Smaller TEX_{86} sea SST increases are seen at the Western Pacific (ODP site 803) and the North West Atlantic (ODP site 628). The cooling of deep-sea Δ_{47} temperatures during the late Eocene is also seen in the TEX_{86} SST records of Cramwinckel et al., 2018 and Inglis et al., 2015. The temperature increases during the EOT for nearly all sites therefore correlate with the deep-sea Δ_{47} temperatures derived from this research. It must be noted that that the TEX_{86} sample size is small and contain hiatuses (Inglis et al., 2015; Cramwinckel et al., 2018). TEX_{86} temperature calibrations are also dependent of the characteristics of different species degradation of organic matter and transport (Conte, 1995; Huguet et al., 2009).

Significant is the CO_2 decline during the late Eocene and EOT and the CO_2 increase in the early Oligocene (Pearson et al., 2009). The CO_2 decline during the late Eocene led to global cooling and the formation of sea ice around Antarctica (Cramwinckel et al., 2018; Goldner et al., 2014). This corresponds with the deep-sea Δ_{47} temperatures. However, a mismatch is seen during the EOT, where the deep-sea Δ_{47} temperatures rose and the CO_2 declined (Pearson et al., 2009). This mismatch can be explained by differences in the age models, the general trend does correlate with the derived deep-sea Δ_{47} temperatures.

CO_2 and benthic $\delta^{18}O$ are normally always in a synchronous relation via temperature, yet they show a mismatch as well (Hansen et al., 2013). The $\delta^{18}O$ temperatures from this research suggest a rapid decline in temperature during the EOT with low temperatures after, this does not correlate with the increasing CO_2 values during the early Oligocene (Pearson et al., 2009). Small shifts in CO_2 values normally leads to large ice-volume changes (Stap et al., 2016). This agrees with the deep-sea Δ_{47} temperatures of this research, since the $\delta^{18}O_{sw}$ shifts from nearly ice-free values to values close to the LGM. The ice volume must therefore contribute less to the $\delta^{18}O$ values, since deep-sea Δ_{47} temperatures show low temperatures during the late Eocene and the $\delta^{18}O_{sw}$ reaches values close to an assumed ice-free world. It is assumed ice sheets were already present in the late Eocene, meaning that other factors must contribute to $\delta^{18}O_{sw}$ fluctuations (Stap et al., 2016; Ladant et al., 2014; Scher et al., 2011). It can therefore be stated that previous deep-sea temperature reconstructions according to $\delta^{18}O$ values need to be re-evaluated.

A

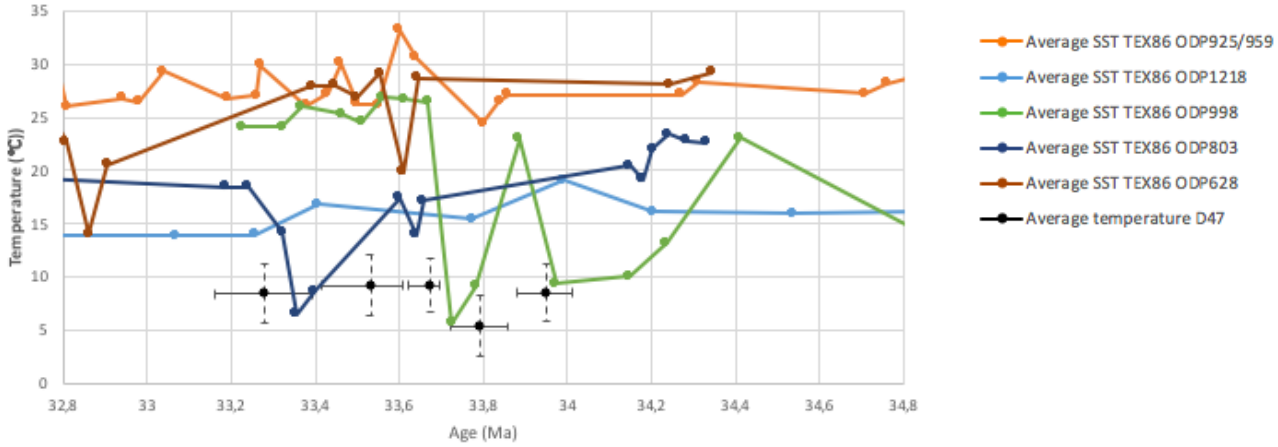

B

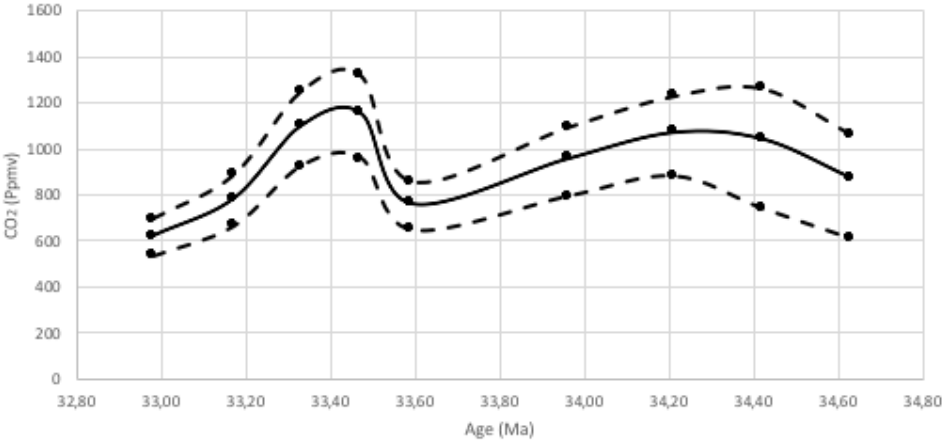

C

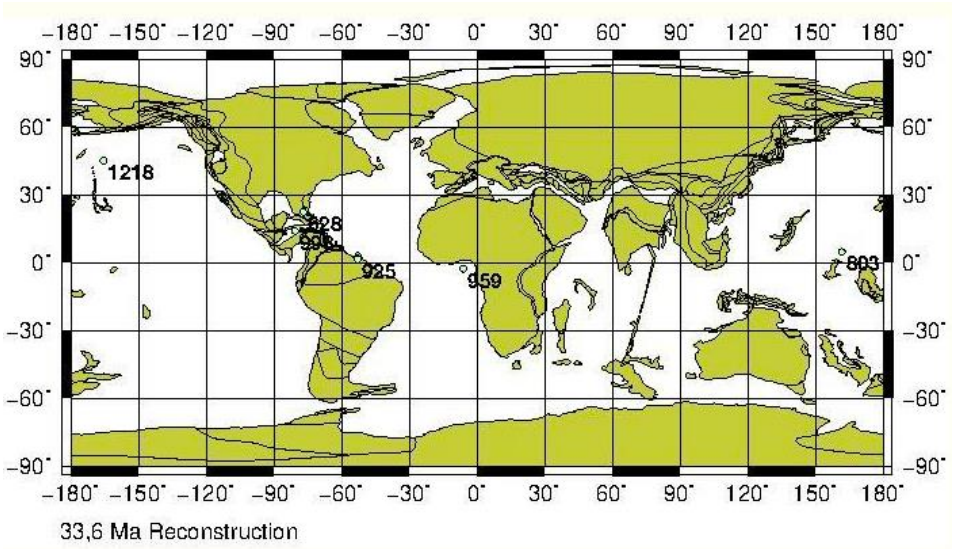

Figure 4.3: A: Sea surface temperatures derived from TEX86 data compared to deep-water temperatures from this research. TEX86 calculated SST acquired through Cramwinckel et al., 2018 (ODP Site 925/959) and Inglis et al., 2015 (ODP Site 1218, 998, 803, 628) B: CO_2 record from boron isotopic data in *T. ampliapertura* in ppm (Pearson et al., 2009). Dotted lines indicate the 95% interval. C: Reconstructed map during EOT with the locations of the ODP sites from where TEX86 data is derived.

4.4 The effect of circulation and water masses on δ^{18}Osw values

The increase of $\delta^{18}O_{sw}$ during the EOT can be explained by multiple factors. As discussed before, the increase of $\delta^{18}O_{sw}$ from almost assumed ice-free values to values close to the LGM provides evidence for the presence and extension of ice sheets (Clark & Mix, 2002). Since the deep-sea Δ_{47} temperature increased during the EOT and the $\delta^{18}O_{sw}$ shifted to values close to the LGM, other factors than ice sheet formation must have contributed to the increase of $\delta^{18}O_{sw}$. This research proposes the idea of $\delta^{18}O_{sw}$ shifts because of density changes in the ocean. $\delta^{18}O_{sw}$ and salinity are correlated within the oceans since they both reflect evaporation and freshwater inflows to the ocean surface (Lynch-Stieglitz et al., 1999). A change in ocean circulation in combination with salinity shifts can therefore be a mechanism that explains the offset between $\delta^{18}O$ and deep-sea Δ_{47} temperatures (Agterhuis et al., 2022).

The decrease of CO_2 as shown by Pearson et al., 2009 result in cooling of the surface waters (Maier-Reimer et al., 1996). This evidence is supported by the TEX_{86} data as discussed in the previous section. The presence of ice sheets and sea ice increases the planetary albedo and therefore also decreases the global SST (Rahmstorf, 2002). The global cooling of SST creates higher density surface waters, which sink to the bottom of the ocean and cause alterations in the ocean circulation (Huber & Sloan, 2001). The increase of temperature during the EOT according to deep-sea Δ_{47} temperatures and TEX_{86} data resulted in higher CO_2 values after. Higher temperatures and higher CO_2 values result in increased evaporation for the oceans and therefore higher saline waters, which sink to intermediate depths (Huber and Sloan, 2001). Since $^{18}O_{sw}$ and salinity are correlated, the intermediate waters will have higher $^{18}O_{sw}$ values (Lynch-Stieglitz et al., 1999). Extremely high temperatures as seen during the PETM will result in the reversal of the ocean circulation, while extremely low temperatures can result in a complete shutdown (Lunt et al., 2010; Jackson et al., 2015).

As discussed before, it is likely that the decreasing CO_2 during the late Eocene and the EOT resulted in lowering of the global SST (Maier-Reimer et al., 1996). Due to the opening of the Southern Ocean gateways, Antarctica was isolated and no heat influx occurred (Baatsen et al., 2018). This enhanced the growth of sea ice around Antarctica, which lowered the salinity and thus the density (Goldner et al., 2014). The sea ice increased the topography around Antarctica and a pressure gradient between Antarctica and the South Atlantic Ocean Current was created, resulting in increased Ekman transport with salt fluxes to the Antarctic Circumpolar Current (ACC; Goldner et al., 2014; Houben et al., 2019). This increased the vertical mixing and deep-water formation around Antarctica (Scher & Martin, 2006). The decrease of $\delta^{18}O_{sw}$ during the late Eocene can therefore likely be explained by the increased polar flow of the more saline deep water of the Atlantic Meridional Overturning Circulation (AMOC; Houben et al., 2019).

The deep-sea derived Δ_{47} temperatures increased during the EOT and corresponds with an increase in $\delta^{18}O_{sw}$. Increasing global temperatures during the EOT resulted in enhanced evaporation and therefore more saline waters in the South Atlantic Ocean (Huber and Sloan, 2001). It is likely that the increased global temperatures melted the Antarctic sea ice and caused meltwater inflow in the ACC, which reduced the pressure gradient. Thus, more saline intermediate waters were formed and less Ekman transport to the ACC occurred, which resulted in an increase of $^{18}O_{sw}$ during the EOT (Huber and Sloan, 2001; Lynch-Stieglitz et al., 1999). This mechanism can explain that $\delta^{18}O_{sw}$ is less dependent on global temperature and ocean circulation may have had a big impact on the seawater chemistry.

4.5 Long-term deep-sea ocean temperatures during the Cenozoic

In this section, the deep-sea derived Δ_{47} temperatures are compared to the long-term deep-sea Δ_{47} temperatures of Meckler et al., 2022. This has been done to see if the Δ_{47} temperatures of this research correlate with the long-term deep-sea derived Δ_{47} temperatures during the Cenozoic. The results are shown in figure 4.4.

The deep-sea derived Δ_{47} temperatures of Meckler et al., 2022 show an overall decreasing trend during the Eocene (56 Ma – 34 Ma; Meckler et al., 2022). A rapid decrease in the Δ_{47} temperature of Meckler et al., 2022 can be seen around ±36.4 – 35.6 Ma and ±35.5 – 33.8 Ma, followed by an increase in temperature during the EOT. This corresponds with the deep-sea derived Δ_{47} temperatures from this research, where also a decrease in temperature in the late Eocene was seen and followed by an increase of temperature during the EOT. It can therefore be stated that the Δ_{47} derived temperatures from this research fit in the global long-term Δ_{47} deep-sea temperature trend.

The global cooling trend since the Early Eocene Climatic Optimum (EECO; 52-50 Ma) is reflected in the Meckler et al., 2022 data and is likely caused by the opening of the Southern Ocean gateways and declining atmospheric CO_2 concentrations (Bijl et al., 2013). The major cooling trend in the Eocene occurred right after the EECO according to the Meckler et al., 2022 data and not during the EOT. The rapid decline in temperature during the Eocene therefore supports the hypothesis of the formation and growth of ice caps during the Eocene and not just during the EOT (Ladant et al., 2014).

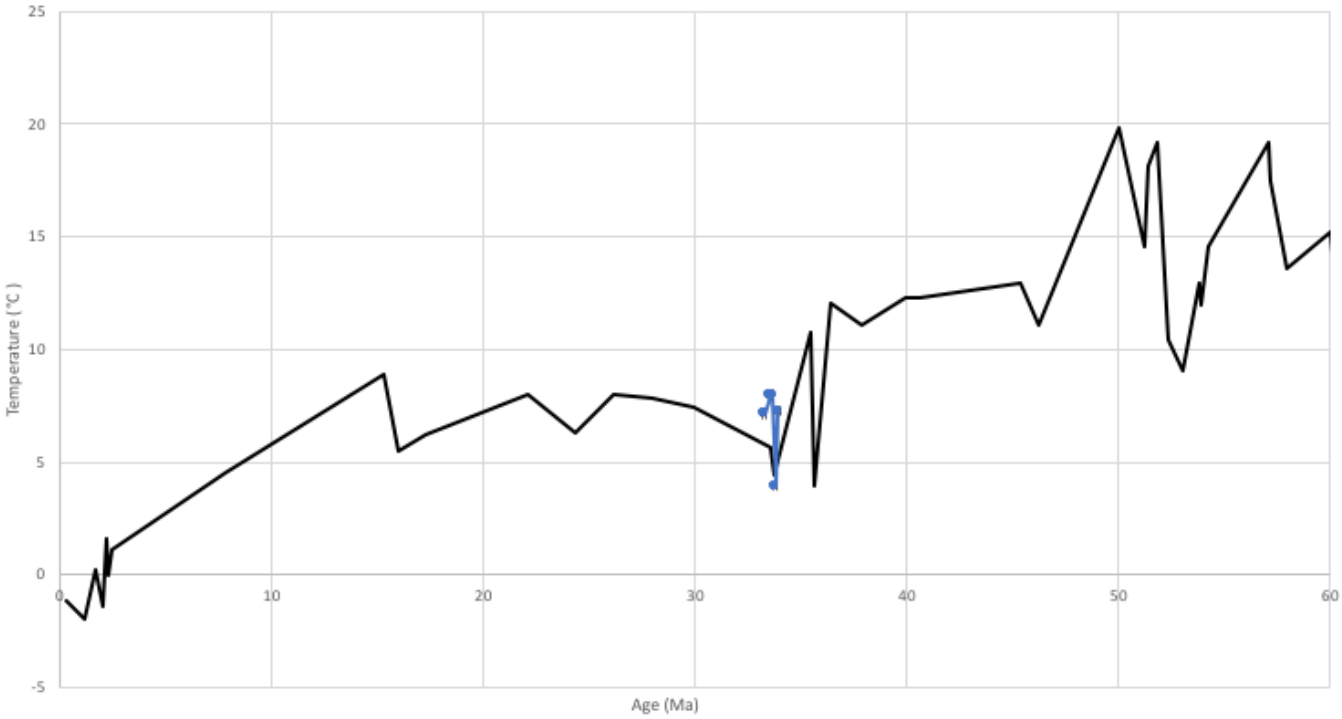

Figure 4.4: Cenozoic Δ_{47} derived deep-sea temperatures of Meckler et al., 2022 in black compared to Δ_{47} derived deep-sea temperatures of this research during the EOT in blue.

4.6 Global mean surface temperature

The global mean surface temperature (GMST) is commonly estimated by the use of $\delta^{18}O$ temperatures (Inglis et al., 2020). As discussed before, $\delta^{18}O$ temperatures might be highly uncertain and therefore give inaccurate results for the GMST. Here we estimate the GMST by using the Δ_{47} temperature derived by the Peral et al., 2022 calibration from this research. The equations are derived from Hansen et al., 2013 and follow the assumptions made in that research.

It is assumed that changes in the GMST prior to the Pliocene-Pleistocene boundary (5.33 Ma) are equal to changes in the bottom water temperature (BWT; Hansen et al., 2013). This equals to equation 4.1 and 4.2.

(4.1) $\Delta GMST = \Delta BWT$

(4.2) $GMST_{dataset} - GMST_{Pliocene} = BWT_{dataset} - BWT_{Pliocene}$

- Where $GMST_{dataset}$ and $GMST_{Pliocene}$ are the global mean surface temperatures per bin of the dataset and the Pliocene
- Where $BWT_{dataset}$ and $BWT_{Pliocene}$ are the bottom water temperatures for the different bins of the dataset and the Pliocene

$BWT_{Pliocene.}$is derived from the 5.33 Ma boundary of Hansen et al., 2013 and is estimated at a value of ±2.0°C. Since climate models showed values biased towards summer, which required extremely high CO_2 levels, a correction for the $BWT_{Pliocene}$ was made (Hansen et al., 2013). Equation 4.3 shows the calculation with the correction for $GMST_{Pliocene}$.

(4.3) $GMST_{Pliocene} = 2.5 \times BWT_{Pliocene} + 12.15$

The GMST is plotted in figure 4.5 and compared against the global CO_2 trend. The GMST does not correlate with the global CO_2 during the EOT. A global CO_2 decrease is seen, while the GMST increased according to the Δ_{47} temperatures. When looking at the 95% intervals, the general trend can possibly correlate, but there is not enough evidence to support that claim.

A

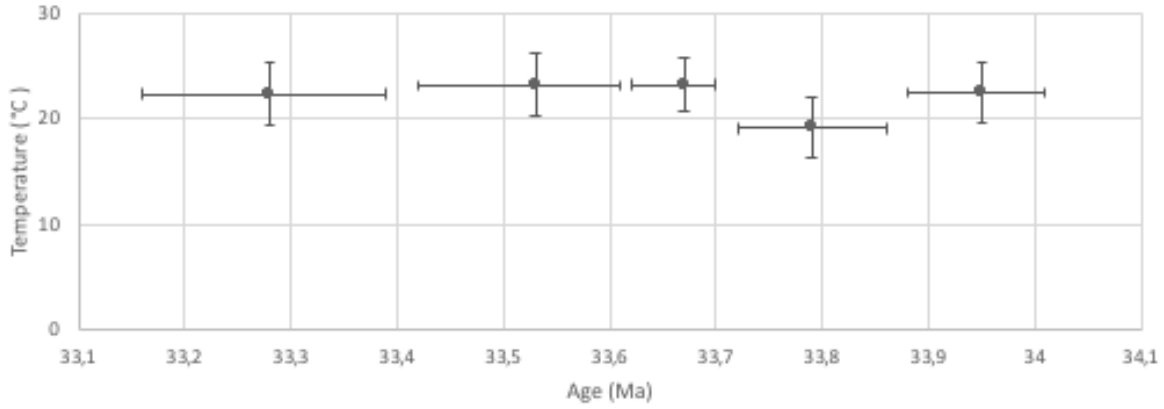

B

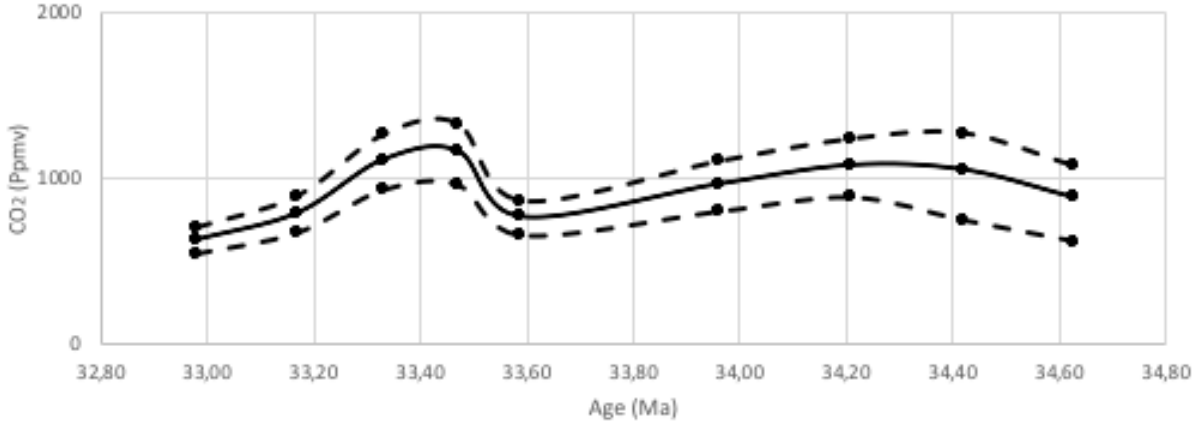

Figure 4.4: A: GMST over time by using the GMST calculation of Hansen et al., 2013 with vertical 95% confidence interval. B: CO_2 record from boron isotopic data in *T. ampliapertura* in ppm (Pearson et al., 2009). Dotted lines indicate the 95% interval.

Conclusions

It can be concluded that the traditional proxies used for climate reconstructions, such as stable oxygen isotopes, Mg/Ca ratios and TEX_{86}, contain limitations and uncertainties. This study proposes a more reliable proxy for reconstructing deep ocean temperature and the global mean surface temperature, the clumped isotope (Δ_{47}) thermometer. Clumped isotopes offer the advantage of being independent of seawater chemistry and specific physiological characteristics of foraminifera.

This research is based on sediment cores from the Walvis Ridge (ODP Leg 208, site 1263) and demonstrates the discrepancies and uncertainties associated with traditional proxies. Comparisons between Δ_{47} temperatures and $\delta^{18}O$ and Mg/Ca temperatures results in significant differences and offsets. The temperature offset between $\delta^{18}O$ and Δ_{47} can be explained by the dependence of $\delta^{18}O$ on seawater chemistry, foraminifera physiology and the pH effect. The Mg/Ca temperatures are also highly uncertain due seawater Mg/Ca fluctuations, hiatuses and variations in the H exponent. The Δ_{47} temperatures show an increase of ±3.9 °C (Meinicke calibration) and ±4.1 °C (Peral calibration) during the EOT, unlike traditional oxygen isotope temperatures which show a rapid decrease in temperatures.

Δ_{47} temperatures derived in this study offer a more plausible reconstruction of deep ocean temperatures. According to CO_2 data from other researches and the derived $\delta^{18}O_{sw}$ values from this research, it can be stated that there were already ice sheets present during the Eocene and they extended in size during the EOT without being dependent of temperature. It is likely that the $\delta^{18}O_{sw}$ is not just influenced by ice sheet formation, but also by factors such as salinity of the seawater, the storage of $\delta^{16}O$ in continental aquifers and seafloor spreading rates. Comparisons between Δ_{47} temperatures and TEX_{86} derived temperatures support this evidence.

Overall, the clumped isotope (Δ_{47}) thermometer is a useful proxy for reconstructing deep ocean temperatures and GMST and offers a promising approach to understand the dynamics of the climate during the EOT. The findings of this study support the evidence of the presence of ice sheets during the Eocene and the extension of the ice sheets during the EOT, despite the increasing temperatures. Further research like pH influence on benthic foraminifera and modernizing of proxy methodologies are necessary to improve the understanding of past climate variations and implications for future climate scenarios.

Acknowledgements

I want to thank my supervisors for their assistance and feedback. Especially my daily supervisor Tobias Agterhuis who guided me through this research and was always available for questions and help. I also want to thank Lucas Lourens and Martin Ziegler for their feedback and guidance and Natasja Welters and Giovanni Dammers for their assistance in the GeoLab of the Utrecht University.

Appendix: Foraminifera glossary

List of definitions of the foraminifera morphology, created by using the Atlas of Benthic Foraminifera by Holbourn, Henderson and Macleod (2013)

Aperture: opening of the test to the exterior

Biconvex: both sides of the test are equally convex

Biumbonate: both sides are umbilical

Evolute: unwinded test with all chambers visible

Interiomarginal slit: opening at margin of the suture of the final chamber

Lenticular: double-convex lens shaped test

Lobulate: chambers are an extension of the periphery with a fold-like structure

Narrow equatorial slit: small symmetrical opening against the periphery

Periphery: edge of foraminifera when looked ventrally or dorsally

Spiral side: the side where all twists are visible

Subacute: moderately acute in shape or angle

Test: shell of the foraminifera

Trochospire: spiral folding of chambers, evolute on one side and involute on other

Umbilical side: involute side where only final twist is visible

Umbilicus: space on internal margins of chambers on umbilical side of test

References

Affek, H. P. (2012). Clumped isotope paleothermometry: principles, applications, and challenges. *The Paleontological Society Papers*, *18*, 101-114.

Agterhuis, T., Ziegler, M., de Winter, N. J., & Lourens, L. J. (2022). Warm deep-sea temperatures across Eocene Thermal Maximum 2 from clumped isotope thermometry. *Communications Earth & Environment*, *3*(1), 39.

Alegret, L., & Thomas, E. (2007). Deep-sea environments across the Cretaceous/Paleogene boundary in the eastern South Atlantic Ocean (ODP leg 208, Walvis Ridge). *Marine Micropaleontology*, *64*(1-2), 1-17.

Baatsen, M. L. J., von der Heydt, A. S., Kliphuis, M., Viebahn, J., & Dijkstra, H. A. (2018). Multiple states in the late Eocene ocean circulation. *Global and Planetary Change*, *163*, 18-28.

Bernasconi, S. M., Daëron, M., Bergmann, K. D., Bonifacie, M., Meckler, A. N., Affek, H. P., ... & Ziegler, M. (2021). InterCarb: A community effort to improve interlaboratory standardization of the carbonate clumped isotope thermometer using carbonate standards. *Geochemistry, Geophysics, Geosystems*, *22*(5), e2020GC009588.

Bijl, P. K., Bendle, J. A., Bohaty, S. M., Pross, J., Schouten, S., Tauxe, L., ... & Yamane, M. (2013). Eocene cooling linked to early flow across the Tasmanian Gateway. *Proceedings of the National Academy of Sciences*, *110*(24), 9645-9650.

Bijl, P. K., Schouten, S., Sluijs, A., Reichart, G. J., Zachos, J. C., & Brinkhuis, H. (2009). Early Palaeogene temperature evolution of the southwest Pacific Ocean. *Nature*, *461*(7265), 776-779.

Bordiga, M., Henderiks, J., Tori, F., Monechi, S., Fenero, R., & Thomas, E. (2015). The Eocene–Oligocene transition at ODP Site 1263, Atlantic Ocean: decreases in nannoplankton size and abundance and correlation with benthic foraminiferal assemblages. *Climate of the Past Discussions*, *11*(3), 1615-1664.

Bordiga, M., Sulas, C., & Henderiks, J. (2017). Reticulofenestra daviesii: Biostratigraphy and paleogeographic distribution across the Eocene–Oligocene boundary. *Geobios*, *50*(5-6), 349-358.

Change, C. (1990). the IPCC scientific assessment. *Houghton JT, Jenkins G, Ephraums JJ eds*, *1*, 990.

Clark, P. U., & Mix, A. C. (2002). Ice sheets and sea level of the Last Glacial Maximum. *Quaternary Science Reviews*, *21*(1-3), 1-7.

Conrad, C. P., & Lithgow-Bertelloni, C. (2007). Faster seafloor spreading and lithosphere production during the mid-Cenozoic. *Geology*, *35*(1), 29-32.

Conte, M. H., Thompson, A., Eglinton, G., & Green, J. C. (1995). Lipid biomarker diversity in the coccolithophorid Emiliania huxleyi (prymnesiophyceae) and the related species Gephyrocapsa oceanica 1. *Journal of Phycology*, *31*(2), 272-282.

Coxall, H. K., & Pearson, P. N. (2007). The Eocene-Oligocene transition. *Deep time perspectives on climate change: Marrying the signal from computer models and biological proxies*, 351-387.

Cramer, B. S., Toggweiler, J. R., Wright, J. D., Katz, M. E., & Miller, K. G. (2009). Ocean overturning since the Late Cretaceous: Inferences from a new benthic foraminiferal isotope compilation. *Paleoceanography*, *24*(4).

Cramer, B. S., Miller, K. G., Barrett, P. J., & Wright, J. D. (2011). Late Cretaceous–Neogene trends in deep ocean temperature and continental ice volume: Reconciling records of benthic foraminiferal geochemistry (δ18O and Mg/Ca) with sea level history. *Journal of Geophysical Research: Oceans*, *116*(C12).

Cramwinckel, M. J., Huber, M., Kocken, I. J., Agnini, C., Bijl, P. K., Bohaty, S. M., ... & Sluijs, A. (2018). Synchronous tropical and polar temperature evolution in the Eocene. *Nature*, *559*(7714), 382-386.

Eiler, J. M. (2007). “Clumped-isotope” geochemistry—The study of naturally-occurring, multiply-substituted isotopologues. *Earth and planetary science letters*, *262*(3-4), 309-327.

Evans, D., & Müller, W. (2012). Deep time foraminifera Mg/Ca paleothermometry: Nonlinear correction for secular change in seawater Mg/Ca. *Paleoceanography*, *27*(4).

Evans, D., Sagoo, N., Renema, W., Cotton, L. J., Müller, W., Todd, J. A., ... & Affek, H. P. (2018). Eocene greenhouse climate revealed by coupled clumped isotope-Mg/Ca thermometry. *Proceedings of the National Academy of Sciences*, *115*(6), 1174-1179.

Ghosh, P., Adkins, J., Affek, H., Balta, B., Guo, W., Schauble, E. A., ... & Eiler, J. M. (2006). 13C–18O bonds in carbonate minerals: a new kind of paleothermometer. *Geochimica et Cosmochimica Acta*, *70*(6), 1439-1456.

Goldner, A., Herold, N., & Huber, M. (2014). Antarctic glaciation caused ocean circulation changes at the Eocene–Oligocene transition. *Nature*, *511*(7511), 574-577.

Hansen, J., Sato, M., Russell, G., & Kharecha, P. (2013). Climate sensitivity, sea level and atmospheric carbon dioxide. *Philosophical Transactions of the Royal Society A: Mathematical, Physical and Engineering Sciences*, *371*(2001), 20120294.

He, B., Olack, G. A., & Colman, A. S. (2012). Pressure baseline correction and high-precision CO2 clumped-isotope (Δ 47) measurements in bellows and micro-volume modes. *Rapid Communications in Mass Spectrometry*, *26*(24), 2837-2853.

Holbourn, A.E., Henderson, A.S., & N. MacLeod. (2013). Atlas of benthic foraminifera. Oxford, UK: Wiley-Blackwell. https://doi.org/10.1002/9781118452493.

Hollis, C. J., Dunkley Jones, T., Anagnostou, E., Bijl, P. K., Cramwinckel, M. J., Cui, Y., ... & Lunt, D. J. (2019). The DeepMIP contribution to PMIP4: methodologies for selection, compilation and analysis of latest Paleocene and early Eocene climate proxy data, incorporating version 0.1 of the DeepMIP database. *Geoscientific Model Development*, *12*(7), 3149-3206.

Houben, A. J., Bijl, P. K., Sluijs, A., Schouten, S., & Brinkhuis, H. (2019). Late Eocene Southern Ocean cooling and invigoration of circulation preconditioned Antarctica for full-scale glaciation. *Geochemistry, Geophysics, Geosystems*, *20*(5), 2214-2234.

Huber, M., & Sloan, L. C. (2001). Heat transport, deep waters, and thermal gradients: Coupled simulation of an Eocene greenhouse climate. *Geophysical Research Letters*, *28*(18), 3481-3484.

Huguet, C., Kim, J. H., de Lange, G. J., Damsté, J. S. S., & Schouten, S. (2009). Effects of long term oxic degradation on the U37K′, TEX86 and BIT organic proxies. *Organic Geochemistry*, *40*(12), 1188-1194.

Huntington, K. W., Eiler, J. M., Affek, H. P., Guo, W., Bonifacie, M., Yeung, L. Y., ... & Came, R. (2009). Methods and limitations of ‘clumped’CO2 isotope (Δ47) analysis by gas-source isotope ratio mass spectrometry. *Journal of Mass Spectrometry*, *44*(9), 1318-1329.

Inglis, G. N., Bragg, F., Burls, N. J., Cramwinckel, M. J., Evans, D., Foster, G. L., ... & Pancost, R. D. (2020). Global mean surface temperature and climate sensitivity of the early Eocene Climatic Optimum (EECO), Paleocene–Eocene Thermal Maximum (PETM), and latest Paleocene. *Climate of the Past*, *16*(5), 1953-1968.

Inglis, G. N., Farnsworth, A., Lunt, D., Foster, G. L., Hollis, C. J., Pagani, M., ... & Pancost, R. D. (2015). Descent toward the Icehouse: Eocene sea surface cooling inferred from GDGT distributions. *Paleoceanography*, *30*(7), 1000-1020.

Jackson, L. C., Kahana, R., Graham, T., Ringer, M. A., Woollings, T., Mecking, J. V., & Wood, R. A. (2015). Global and European climate impacts of a slowdown of the AMOC in a high resolution GCM. *Climate dynamics*, *45*, 3299-3316.

Katz, M. E., Miller, K. G., Wright, J. D., Wade, B. S., Browning, J. V., Cramer, B. S., & Rosenthal, Y. (2008). Stepwise transition from the Eocene greenhouse to the Oligocene icehouse. *Nature geoscience*, *1*(5), 329-334.

Kocken, I. J., Müller, I. A., & Ziegler, M. (2019). Optimizing the use of carbonate standards to minimize uncertainties in clumped isotope data. *Geochemistry, Geophysics, Geosystems*, *20*(11), 5565-5577.

Ladant, J. B., Donnadieu, Y., Lefebvre, V., & Dumas, C. (2014). The respective role of atmospheric carbon dioxide and orbital parameters on ice sheet evolution at the Eocene-Oligocene transition. *Paleoceanography*, *29*(8), 810-823.

Langton, S. J., Rabideaux, N. M., Borrelli, C., & Katz, M. E. (2016). Southeastern Atlantic deep-water evolution during the late-middle Eocene to earliest Oligocene (Ocean Drilling program site 1263 and Deep Sea Drilling project site 366). *Geosphere*, *12*(3), 1032-1047.

Lear, C. H., Mawbey, E. M., & Rosenthal, Y. (2010). Cenozoic benthic foraminiferal Mg/Ca and Li/Ca records: Toward unlocking temperatures and saturation states. *Paleoceanography*, *25*(4).

Lunt, D. J., Valdes, P. J., Jones, T. D., Ridgwell, A., Haywood, A. M., Schmidt, D. N., ... & Maslin, M. (2010). CO2-driven ocean circulation changes as an amplifier of Paleocene-Eocene thermal maximum hydrate destabilization. *Geology*, *38*(10), 875-878.

Lynch-Stieglitz, J., Curry, W. B., & Slowey, N. (1999). A geostrophic transport estimate for the Florida Current from the oxygen isotope composition of benthic foraminifera. *Paleoceanography*, *14*(3), 360-373.

Maier-Reimer, E., Mikolajewicz, U., & Winguth, A. (1996). Future ocean uptake of CO2: interaction between ocean circulation and biology. *Climate Dynamics*, *12*, 711-722.

Marchitto, T. M., Curry, W. B., Lynch-Stieglitz, J., Bryan, S. P., Cobb, K. M., & Lund, D. C. (2014). Improved oxygen isotope temperature calibrations for cosmopolitan benthic foraminifera. *Geochimica et Cosmochimica Acta*, *130*, 1-11.

Meckler, A. N., Sexton, P. F., Piasecki, A. M., Leutert, T. J., Marquardt, J., Ziegler, M., ... & Bernasconi, S. M. (2022). Cenozoic evolution of deep ocean temperature from clumped isotope thermometry. *Science*, *377*(6601), 86-90.

Meinicke, N., Reimi, M. A., Ravelo, A. C., & Meckler, A. N. (2021). Coupled Mg/Ca and clumped isotope measurements indicate lack of substantial mixed layer cooling in the Western Pacific Warm Pool during the last~ 5 million years. *Paleoceanography and Paleoclimatology*, *36*(8), e2020PA004115.

Miller, K. G., Wright, J. D., & Browning, J. V. (2005). Visions of ice sheets in a greenhouse world. *Marine Geology*, *217*(3-4), 215-231.

Miller, K. G., Browning, J. V., Schmelz, W. J., Kopp, R. E., Mountain, G. S., & Wright, J. D. (2020). Cenozoic sea-level and cryospheric evolution from deep-sea geochemical and continental margin records. *Science advances*, *6*(20), eaaz1346.

O'Connor, J. M., & Duncan, R. A. (1990). Evolution of the Walvis Ridge-Rio Grande Rise hot spot system: Implications for African and South American plate motions over plumes. *Journal of Geophysical Research: Solid Earth*, *95*(B11), 17475-17502.

Passey, B. H., Levin, N. E., Cerling, T. E., Brown, F. H., & Eiler, J. M. (2010). High-temperature environments of human evolution in East Africa based on bond ordering in paleosol carbonates. *Proceedings of the National Academy of Sciences*, *107*(25), 11245-11249.

Pearson, P. N., Ditchfield, P. W., Singano, J., Harcourt-Brown, K. G., Nicholas, C. J., Olsson, R. K., ... & Hall, M. A. (2001). Warm tropical sea surface temperatures in the Late Cretaceous and Eocene epochs. *Nature*, *413*(6855), 481-487.

Pearson, P. N., Foster, G. L., & Wade, B. S. (2009). Atmospheric carbon dioxide through the Eocene–Oligocene climate transition. *Nature*, *461*(7267), 1110-1113.

Peck, V. L., Yu, J., Kender, S., & Riesselman, C. R. (2010). Shifting ocean carbonate chemistry during the Eocene-Oligocene climate transition: Implications for deep-ocean Mg/Ca paleothermometry. *Paleoceanography*, *25*(4).

Peral, M., Bassinot, F., Daëron, M., Blamart, D., Bonnin, J., Jorissen, F., ... & Gray, W. R. (2022). On the combination of the planktonic foraminiferal Mg/Ca, clumped (Δ47) and conventional (δ18O) stable isotope paleothermometers in palaeoceanographic studies. *Geochimica et Cosmochimica Acta*, *339*, 22-34.
Prothero, D. R. (1994). The late eocene-oligocene extinctions. *Annual Review of Earth and Planetary Sciences*, *22*, 145-165.

Petersen, S. V., & Schrag, D. P. (2015). Antarctic ice growth before and after the Eocene-Oligocene transition: New estimates from clumped isotope paleothermometry. *Paleoceanography*, *30*(10), 1305-1317.

Rahmstorf, S. (2002). Ocean circulation and climate during the past 120,000 years. *Nature*, *419*(6903), 207-214.

Rathmann, S., Hess, S., Kuhnert, H., & Mulitza, S. (2004). Mg/Ca ratios of the benthic foraminifera Oridorsalis umbonatus obtained by laser ablation from core top sediments: Relationship to bottom water temperature. *Geochemistry, Geophysics, Geosystems*, *5*(12).

Ravelo, A. C., & Hillaire-Marcel, C. (2007). Chapter eighteen the use of oxygen and carbon isotopes of foraminifera in paleoceanography. *Developments in marine geology*, *1*, 735-764.

Rohling, E. J. (2013). Oxygen isotope composition of seawater. *The Encyclopedia of Quaternary Science. Amsterdam: Elsevier*, *2*, 915-922.

Sames, B., Wagreich, M., Conrad, C. P., & Iqbal, S. (2020). Aquifer-eustasy as the main driver of short-term sea-level fluctuations during Cretaceous hothouse climate phases. *Geological Society, London, Special Publications*, *498*(1), 9-38.

Scher, H. D., Bohaty, S. M., Zachos, J. C., & Delaney, M. L. (2011). Two-stepping into the icehouse: East Antarctic weathering during progressive ice-sheet expansion at the Eocene–Oligocene transition. *Geology*, *39*(4), 383-386.

Scher, H. D., & Martin, E. E. (2006). Timing and climatic consequences of the opening of Drake Passage. *science*, *312*(5772), 428-430.

Schou, J. (1980). Transport theory for kinetic emission of secondary electrons from solids. *Physical Review B*, *22*(5), 2141.

Schrag, D. P., Adkins, J. F., McIntyre, K., Alexander, J. L., Hodell, D. A., Charles, C. D., & McManus, J. F. (2002). The oxygen isotopic composition of seawater during the Last Glacial Maximum. *Quaternary Science Reviews*, *21*(1-3), 331-342.

Spencer, C., & Kim, S. T. (2015). Carbonate clumped isotope paleothermometry: a review of recent advances in CO 2 gas evolution, purification, measurement and standardization techniques. *Geosciences Journal*, *19*, 357-374.

Stap, L. B., Van De Wal, R. S., De Boer, B., Bintanja, R., & Lourens, L. J. (2016). The MMCO-EOT conundrum: Same benthic δ18O, different CO2. *Paleoceanography*, *31*(9), 1270-1282.

Tripati, A., & Darby, D. (2018). Evidence for ephemeral middle Eocene to early Oligocene Greenland glacial ice and pan-Arctic sea ice. *Nature communications*, *9*(1), 1038.

Uchikawa, J., & Zeebe, R. E. (2010). Examining possible effects of seawater pH decline on foraminiferal stable isotopes during the Paleocene-Eocene Thermal Maximum. *Paleoceanography*, *25*(2).

Wang, Z., Schauble, E. A., & Eiler, J. M. (2004). Equilibrium thermodynamics of multiply substituted isotopologues of molecular gases. *Geochimica et Cosmochimica Acta*, *68*(23), 4779-4797.

Wendler, J. E., Wendler, I., Vogt, C., & Kuss, J. (2016). Link between cyclic eustatic sea-level change and continental weathering: Evidence for aquifer-eustasy in the Cretaceous. *Palaeogeography, Palaeoclimatology, Palaeoecology*, *441*, 430-437.

Westerhold, T., Röhl, U., Frederichs, T., Bohaty, S. M., & Zachos, J. C. (2015). Astronomical calibration of the geological timescale: closing the middle Eocene gap. *Climate of the Past*, *11*(9), 1181-1195.

Westerhold, T., Marwan, N., Drury, A. J., Liebrand, D., Agnini, C., Anagnostou, E., ... & Zachos, J. C. (2020). An astronomically dated record of Earth's climate and its predictability over the last 66 million years. *Science*, *369*(6509), 1383-1387.

Zachos, J. C., Stott, L. D., & Lohmann, K. C. (1994). Evolution of early Cenozoic marine temperatures. *Paleoceanography*, *9*(2), 353-387.

Zachos, J. C., Kroon, D., Blum, P., Bowles, J., Gaillot, P., Hasegawa, T., ... & Vallius, H. (2004, August). Early Cenozoic extreme Climates: The Walvis Ridge transect, Proceedings of the Ocean Drilling Program, Initial reports Leg 208. In *Proceedings of the Ocean Drilling Program: Initial Reports*.

Zachos, J. C., Dickens, G. R., & Zeebe, R. E. (2008). An early Cenozoic perspective on greenhouse warming and carbon-cycle dynamics. *nature*, *451*(7176), 279-283.

Zeebe, R. E. (2001). Seawater pH and isotopic paleotemperatures of Cretaceous oceans. *Palaeogeography, palaeoclimatology, palaeoecology*, *170*(1-2), 49-57.